Finite Elements in Analysis and Design 134 (2017) 55–67

Contents lists available at ScienceDirect

Finite Elements in Analysis and Design

journal homepage: www.elsevier.com/locate/finel

Mixed Virtual Elements for discrete fracture network simulations☆

Matías Fernando Benedetto[a,b], Andrea Borio[c], Stefano Scialò[c,*]

[a] Universidad de Buenos Aires, Facultad de Ingeniería, Argentina
[b] CONICET - INTECIN, Grupo LMNI. Buenos Aires, Argentina
[c] Dipartimento di Scienze Matematiche, Politecnico di Torino, Corso Duca degli Abruzzi 24, Torino 10129, Italy

ARTICLE INFO

MSC:
65N30
65N50
68U20
86-08

Keywords:
Mixed Virtual Elements
Discrete Fracture Networks
Mixed formulation
Fracture flows
Darcy flows

ABSTRACT

The present work deals with the simulation of the flow in Discrete Fracture Networks (DFN), using the mixed formulation of the Virtual Element Method (VEM) on polygonal conforming meshes. The flexibility of the VEM in handling polygonal meshes is used to easily generate a conforming mesh even in the case of intricate DFNs. Mixed Virtual Elements of arbitrary polynomial accuracy are then used for the discretization of the velocity field. The well posedness of the resulting discrete problem is shown. Numerical results on simple problems are proposed to show convergence properties of the method with respect to known analytic solutions, whereas some tests on fairly complex networks are also reported showing its applicability and effectiveness.

1. Introduction

Effective flow simulations in underground fractured media are strategic in several practical contexts: protection of water resources, geothermal applications, Oil & Gas enhanced production and geological waste storage. All these applications share two possibly conflicting common characteristics: a high accuracy and reliability is required, whereas the uncertainty on the geometry and on the data demands for a huge number of simulations in order to provide probability distributions of the target quantities.

This work considers the problem of simulating the hydraulic head distribution in the subsoil, modeled as a Discrete Fracture Network (DFN) [1–6], which is a randomly generated set of intersecting planar polygons resembling the fractures in a surrounding porous medium. DFNs are usually characterized by enormous geometrical complexities and by the presence of a large number of fractures forming an intricate network of intersections. Many novel numerical approaches have been recently developed, in order to circumvent problems arising in efficient flow simulations in realistic DFNs. One of the main difficulties consists in the meshing process, since conventional approaches rely on the conformity of the mesh at fracture intersections in order to enforce suitable matching conditions. The generation of a mesh conforming to fracture intersections might have a high computational cost, or even fail, as a consequence of the number of geometrical constraints, and could result in poor quality triangulations for the presence of distorted elements. Furthermore, as already mentioned, input data for DFN simulations are derived from probability distribution of soil properties, thus requiring a large number of costly simulation to derive reliable statistics on the quantity of interest.

Recently, a novel code for the simulation of the flow in DFNs with stochastic input data was proposed in [7–9]. In [10,11] the complexity of DFN flow simulations is tackled resorting to dimensional reduction of the problem, removing the unknowns in the interior of the fractures and rewriting the problems at the interfaces. In [12,13] the authors use the eXtended Finite Element Method (XFEM) in order to allow for the presence of interfaces in the domain not conforming to the mesh. The XFEM is also used in [14,15]. In [16–20] the authors suggest the use of an optimization-based approach on non-conforming meshes to avoid any problem related to the generation of the mesh. The proposed optimization approach also provides a scalable resolution algorithm [21], and is used in conjunction with different discretization choices, ranging from standard finite elements, to the XFEM, [22,23], or to the new virtual element method [24]. Recently, techniques as the Mimetic Finite Difference method (MFD, [25,26]) have been used for flow

☆ This research has been partially supported by the Italian MIUR through PRIN research grant 2012HBLYE4_001 *Metodologie innovative nella modellistica differenziale numerica* and by INdAM-GNCS through project *Tecniche numeriche avanzate basate su discretizzazioni con elementi poligonali/poliedrici per contesti applicativi caratterizzati da una elevata complessità geometrica* (2017) and by Politecnico di Torino through project *Starting Grant RTD* (2017).

* Corresponding author.
E-mail addresses: mbenedet@fi.uba.ar (M.F. Benedetto), andrea.borio@polito.it (A. Borio), stefano.scialo@polito.it (S. Scialò).

http://dx.doi.org/10.1016/j.finel.2017.05.011
Received 23 March 2017; Received in revised form 19 May 2017; Accepted 28 May 2017

simulations in DFNs, by [27,28], as an example, and also the new Virtual Element Method (VEM, [29–34]) was proposed, in addition to the already mentioned reference [24], also in [35,36]. In these last two works, in particular, the authors take advantage of the flexibility of virtual elements to easily generate a polygonal mesh of the fracture network that satisfies certain conformity requirements with fracture intersections.

The use of mixed formulation in DFN simulations is a widely common choice, for the possibility of a direct computation of the Darcy velocity; see among others [37,12,38–42,27,28]. This improves the accuracy for simulations in which the velocity is to be used as the transport field of an advection-diffusion process of a passive scalar, as in the case of the evolution of the concentration of a pollutant in the subsoil.

In the present work, the framework proposed in [35] is extended to the use of Mixed Virtual Elements, thus combining the reliable meshing process used therein to the mentioned advantages of the mixed formulation. The continuous advection-diffusion-reaction problem in a DFN is presented in mixed form, introducing suitable matching conditions at fracture intersections for the pressure and velocity fields. The discrete formulation with Mixed Virtual Elements of arbitrary polynomial accuracy is then derived, and a proof of well posedness is also provided. Numerical results on simple DFN configurations are first proposed, showing convergence rates of the numerical solution to the known exact solutions. Polynomial accuracy values ranging from $k = 0$ to $k = 5$ are considered. Afterwards, other numerical tests are shown on increasingly complex networks, in order to highlight the viability and the effectiveness of the method in dealing with realistic DFN configurations.

The presentation follows this outline: in Section 2 we describe the domain of interest, establish some notations and write the continuous model that describes the hydraulic head distribution within the DFN. In Section 3 the discrete formulation of the problem based on the mixed VEMs on each fracture is discussed and suitable coupling conditions at intersections are introduced. Well posedness of the discrete problem is shown. Some notes on the implementation are given in Section 4. Finally, in Section 5 validation tests are shown on advection-diffusion-reaction problems written on simple domains, together with an analysis of the performances of the method in solving pure diffusion problems on realistic DFNs.

We use the notation $\|\cdot\|_{k,\omega}$ to indicate the $\mathbf{H}^k(\omega)$-norm of vectors or scalar functions, on some set $\omega \subset \mathbb{R}^2$. In the case of a vector $\mathbf{v} = (v_1, v_2)$, we intend, e.g., $\| \mathbf{v}^2_{0,\omega} = \| \int_\omega (v_1(x, y)^2 + v_2(x, y)^2)\mathrm{d}x\mathrm{d}y$. Moreover, the symbol $[\![\mathbf{v}\cdot\mathbf{n}_\sigma]\!]_\sigma$ denotes the jump $(\mathbf{v}\cdot\mathbf{n}^+_\sigma) - (\mathbf{v}\cdot\mathbf{n}^-_\sigma)$ across a segment σ, being $\mathbf{n}^+_\sigma$, $\mathbf{n}^-_\sigma$ the unit normal vectors to σ with opposite directions. We have that $\mathbf{n}_\sigma$ is the unit normal vector to σ with one fixed orientation, and we observe that the definition of the jump is independent from the choice of $\mathbf{n}_\sigma$.

2. The continuous problem

The geometrical setting for the problem of interest is a *Discrete Fracture Network* Ω, that is a finite set of planar polygonal *fractures* intersecting in the 3D space. Each fracture in Ω is denoted by F_i, for some index $i = \{1,\dots, N\} = \mathcal{I}$, whereas intersections between fractures are called *traces* and indicated by Γ_ℓ, for $\ell=\{1,\dots, L\} = \mathcal{L}$. We assume, for simplicity, that each intersection occurs between exactly two fractures, and we define, for each $\ell \in \mathcal{L}$, $\mathcal{I}_\ell = (i, j)$, with $i < j$, as the ordered couple of indices of those fractures meeting at Γ_ℓ, i.e. $\Gamma_\ell = \overline{F_i} \cap \overline{F_j}$. For each fracture F_i, $\mathcal{L}_i$ is the set of indices of those traces that F_i shares with other fractures.

The boundary of Ω, $\partial\Omega$ is split in a Dirichlet part $\Gamma_D \neq \emptyset$ and a Neumann part Γ_N with $\partial\Omega = \Gamma_D \cup \Gamma_N$ and $\Gamma_D \cap \Gamma_N = \emptyset$. Let us denote by h the hydraulic head in Ω and by h_i its restriction to F_i for $i \in \mathcal{I}$. Let further F_i be subdivided in a set of sub-domains $F_{i,j}$, $j \in \{1,\dots, N_i\}$, such that the traces lying on F_i are now part of the boundary of some of these sub-domains. Then, the hydraulic head h in Ω is the solution of the following system of equations, which, for $i \in \mathcal{I}$ and $j \in \{1,\dots, N_i\}$ reads as:

$$\begin{cases} \mathrm{div}(-\mathrm{K}_i\nabla h_i + \mathbf{b}_i h_i) + \gamma_i h_i = f_i & \text{in } F_{i,j}, \\ h_i = h_{Di} & \text{on } \Gamma_{Di} \cap \partial F_{i,j}, \\ (-\mathrm{K}_i\nabla h_i + \mathbf{b}_i h_i)\cdot \mathbf{n}_{\Gamma_{Ni}} = h_{Ni} & \text{on } \Gamma_{Ni} \cap \partial F_{i,j}, \end{cases} \tag{1}$$

where K_i is a uniformly positive definite tensor expressing the transmissivity of fracture F_i, whereas $\partial F_{i,j}$ is the boundary of $F_{i,j}$, and ∂F_i is the boundary of F_i which is split in a Dirichlet part $\Gamma_{Di} = \Gamma_D \cap \partial F_i$ on which the value h_{Di} is prescribed and a Neumann part $\Gamma_{Ni} = \Gamma_N \cap \partial F_i$. Across Γ_{Ni} a total (diffusive and advective) flux is imposed equal to h_{Ni}. Finally ${}^{\mathbf{n}}\Gamma_{Ni}$ is the outward unit normal vector to the Neumann boundary.

Problems on the fractures are coupled together by natural matching conditions expressing the continuity of h at traces and the balance of fluxes: for all $\ell \in \mathcal{L}$, if $\mathcal{I}_\ell = (i, j)$,

$$h_i|_{\Gamma_\ell} - h_j|_{\Gamma_\ell} = 0, \tag{2}$$

$$\frac{\partial h_i}{\partial \mathbf{n}^i_{\Gamma_\ell}} + \frac{\partial h_j}{\partial \mathbf{n}^j_{\Gamma_\ell}} = 0. \tag{3}$$

where $\mathbf{n}^i_{\Gamma_\ell}$ is the unit normal vector to Γ_ℓ with a fixed orientation on F_i.

In order to introduce the variational formulation of problem (1), let us set the following functional spaces: for $i \in \mathcal{I}$ and $j = 1,\dots, N_i$,

$$\mathrm{H}(\mathrm{div}, \mathrm{F}_{i,j}) := \left\{ \mathbf{v} \in [\mathrm{L}^2(F_{i,j})]^2 : \mathrm{div}(\mathbf{v}) \in \mathrm{L}^2(F_{i,j}) \right\},$$

$$\mathrm{H}_0(\mathrm{div}, \mathrm{F}_{i,j}) := \left\{ \mathbf{v} \in \mathrm{H}(\mathrm{div}, \mathrm{F}_{i,j}) : (\mathbf{v}\cdot\mathbf{n}\Gamma_{\mathrm{Ni}})|_{\partial F_{i,j}} = 0 \right\}.$$

We define

$$\mathbb{V}_{i,0} := \{\mathbf{v}_i := (\mathbf{v}_{i,j})_{j=1,\dots,N_i} : \mathbf{v}_{i,j} \in \mathrm{H}_0(\mathrm{div}, \mathrm{F}_{i,j}) \quad \forall \mathrm{j} \in \{1,\dots, \mathrm{N}_i\}\},$$

$$\mathbb{V}_i := \{\mathbf{v}_i := (\mathbf{v}_{i,j})_{j=1,\dots,N_i} : \mathbf{v}_{i,j} \in \mathrm{H}(\mathrm{div}, \mathrm{F}_{i,j}) \quad \forall \mathrm{j} \in \{1,\dots, \mathrm{N}_i\}\},$$

$$\mathbb{V} := \{\mathbf{v} := (\mathbf{v}_i)_{i=1,\dots,N} : \mathbf{v}_i \in \mathbb{V}_{i,0} \quad \forall i \in \mathcal{I}\},$$

$$\mathbb{Q} := \{q = (q_i)_{i=1,\dots,N} : q_i \in \mathrm{L}^2(F_i) \quad \forall i \in \mathcal{I}\},$$

$$\mathbb{G} := \left\{\mu = (\mu_\ell)_{\ell=1,\dots,M} : \mu_\ell \in \mathrm{H}^{\frac{1}{2}}(\Gamma_\ell) \quad \forall \ell \in \mathcal{L}\right\},$$

endowed with the following natural norms:

$$\|\mathbf{v}\|_{\mathbb{V}_i} := \left(\|\mathbf{v}\|^2_{0,F_i} + \sum_{j=1}^{N_i} \|\mathrm{div}(\mathbf{v})\|^2_{0,F_{i,j}} \right)^{\frac{1}{2}} \quad \forall i \in \mathcal{I}, \mathbf{v} \in \mathbb{V},$$

$$\|\mathbf{v}\|_{\mathbb{V}} := \left(\sum_{i\in\mathcal{I}} \|\mathbf{v}\|^2_{\mathbb{V}_i} \right)^{\frac{1}{2}} \quad \forall \mathbf{v} \in \mathbb{V},$$

$$\|q\|_{\mathbb{Q}} := \left(\sum_{i\in\mathcal{I}} \|q\|^2_{0,F_i} \right)^{\frac{1}{2}} \quad \forall q \in \mathbb{Q},$$

$$\|\mu\|_{\mathbb{G}} := \left(\sum_{\ell\in\mathcal{L}} \|\mu_\ell\|^2_{\frac{1}{2},\Gamma_\ell} \right)^{\frac{1}{2}} \quad \forall \mu \in \mathbb{G},$$

in which $\| v \|_{\ell,\omega}$ denotes, as usual, the norm of function v in $\mathrm{H}^\ell(\omega)$.

By defining $\nu_i := \mathrm{K}_i^{-1}$, $\beta_i := \mathrm{K}_i^{-1}\mathbf{b}_i$, $\forall\, i \in \mathcal{I}$, and introducing, on each fracture F_i, $i \in \mathcal{I}$ the new variables $\mathbf{u}_i := -\mathrm{K}_i\nabla h_i + \mathbf{b}_i h_i$ and for each $\ell \in \mathcal{L}$ formally defining $\lambda_\ell = h|_{\Gamma_\ell}$, we can recast (1) in the following dual variational form:

Find $\mathbf{u} = \mathbf{u}_0 + \mathbf{u}_N$, *with* $\mathbf{u}_0 \in \mathbb{V}$, $h \in \mathbb{Q}$ *and* $\lambda \in \mathbb{G}$ *such that*

$$\begin{cases} a_i(\mathbf{u}_0, \mathbf{v}) - d_i(\mathbf{v}, h) - b_i(h, \mathbf{v}) + g_i(\lambda, \mathbf{v}) = \\ \qquad = -\langle \mathbf{v}_i \cdot \mathbf{n}, h_{Di} \rangle_{\pm\frac{1}{2}, \Gamma_{Di}} - a_i(\mathbf{u}_N, \mathbf{v}) \qquad \forall \mathbf{v} \in \mathbb{V}, \\ d_i(\mathbf{u}_0, q) + c_i(h, q) = (f, q_i)_{F_i} - d_i(\mathbf{u}_N, q) \qquad \forall q \in \mathbb{Q}, \end{cases} \tag{4}$$

where $\mathbf{u}_N$ is any function such that, being $\mathbf{u}_{i,N} = \mathbf{u}_N|_{F_i} \in \mathbb{V}_i$, it is $\mathbf{u}_{i,N} \cdot {}^{\mathbf{n}}\Gamma_{Ni} = h_{Ni}$ and we have defined

$$\begin{aligned} a_i(\mathbf{w}, \mathbf{v}) &:= (\nu \mathbf{w}_i, \mathbf{v}_i)_{F_i} && \forall \mathbf{w}, \mathbf{v} \in \mathbb{V}, \\ b_i(q, \mathbf{v}) &:= (q_i, \beta_i \cdot \mathbf{v}_i)_{F_i} && \forall q \in \mathbb{Q}, \mathbf{v} \in \mathbb{V}, \\ c_i(p, q) &:= (\gamma p_i, q_i)_{F_i} && \forall p, q \in \mathbb{Q}, \end{aligned} \tag{5}$$

$$\begin{aligned} d_i(\mathbf{v}, q) &:= (\mathrm{div}(\mathbf{v}_i), q_i)_{F_i} && \forall \mathbf{v} \in \mathbb{V}, q \in \mathbb{Q}, \\ g_i(\mu, \mathbf{v}) &:= \sum_{\ell \in \mathcal{L}_i} \left\langle [\![\mathbf{v}_i \cdot \mathbf{n}^i_{\Gamma_\ell}]\!]_{\Gamma_\ell}, \mu_\ell \right\rangle_{\pm\frac{1}{2}, \Gamma_\ell} && \forall \mu \in \mathbb{G}, \mathbf{v} \in \mathbb{V}. \end{aligned} \tag{6}$$

Problems (4) on the fractures are coupled by the following variational equations, which follows from (3):

$$\langle \{\{\mathbf{u}\}\}_{\Gamma_\ell}, \lambda_\ell \rangle_{\pm\frac{1}{2}, \Gamma_\ell} = 0 \quad \forall \lambda_\ell \in \mathrm{H}^{\frac{1}{2}}(\Gamma_\ell), \quad \forall \ell \in \mathcal{L}, \tag{7}$$

where, if $\mathcal{I}_\ell = (i, j)$, $\{\{\mathbf{u}\}\}_{\Gamma_\ell} := [\![\mathbf{u}_i \cdot \mathbf{n}^i_{\Gamma_\ell}]\!]_{\Gamma_\ell} + [\![\mathbf{u}_j \cdot \mathbf{n}^j_{\Gamma_\ell}]\!]_{\Gamma_\ell}$. After denoting by:

$$\begin{aligned} a(\mathbf{w}, \mathbf{v}) &:= \sum_{i \in \mathcal{I}} a_i(\mathbf{w}, \mathbf{v}) && \forall \mathbf{w}, \mathbf{v} \in \mathbb{V}, \\ b(q, \mathbf{v}) &:= \sum_{i \in \mathcal{I}} b_i(q, \mathbf{v}) && \forall q \in \mathbb{Q}, \mathbf{v} \in \mathbb{V}, \\ c(p, q) &:= \sum_{i \in \mathcal{I}} c_i(p, q) && \forall p, q \in \mathbb{Q}, \\ d(\mathbf{v}, q) &:= \sum_{i \in \mathcal{I}} d_i(\mathbf{v}, q) && \forall \mathbf{v} \in \mathbb{V}, q \in \mathbb{Q}, \\ g(\mu, \mathbf{v}) &:= \sum_{i \in \mathcal{I}} g_i(\mu, \mathbf{v}) && \forall \mu \in \mathbb{G}, \mathbf{v} \in \mathbb{V}, \end{aligned}$$

problem (4)–(7) can be re-stated as the following system of equations on the whole network: find $\mathbf{u} = \mathbf{u}_0 + \mathbf{u}_N$, with $\mathbf{u}_0 \in \mathbb{V}$, $h \in \mathbb{Q}$ and $\lambda \in \mathbb{G}$ such that

$$\begin{cases} a(\mathbf{u}_0, \mathbf{v}) - b(h, \mathbf{v}) - d(\mathbf{v}, h) + g(\lambda, \mathbf{v}) = \\ \qquad = -(h_D, \mathbf{v} \cdot \mathbf{n})_{\Gamma_D} - a(\mathbf{u}_N, \mathbf{v}) \qquad \forall \mathbf{v} \in \mathbb{V}, \\ d(\mathbf{u}_0, q) + c(h, q) = (f, q) - d(\mathbf{u}_N, q) \qquad \forall q \in \mathbb{Q}, \\ g(\mu, \mathbf{u}_0) = -g(\mu, \mathbf{u}_N) \qquad \forall \mu \in \mathbb{G}. \end{cases} \tag{8}$$

Notice that in the above problem, h is in general discontinuous at fracture intersections, and λ is playing the role of its trace. By classical arguments and assumptions on the regularity of the data, (see e.g. [43]), it can be proven that, if problem (1)–(3) is well posed, (8) has a unique solution, which coincides with the one of (1)–(3) [43,32].

3. The discrete problem with the Mixed Virtual Element Method

The mixed formulation for the Virtual Element Method (VEM) has been recently presented in [30], with a followup work generalizing the method in [32], and, due to its recent introduction, the only work regarding its application, at the time of writing, is [44], which deals with Stokes flow. Here, we use a Mixed VEM space to discretize the velocity space $\mathbb{V}$, while the pressure and trace spaces $\mathbb{Q}$ and $\mathbb{G}$ are discretized in a standard way.

After a brief presentation of the mesh generation process proposed for the present work, a description of the Mixed Virtual Element in the context fo DFN flow simulation is provided. The reader is, however, referred to [30,32] for most of the theoretical results concerning the VEM.

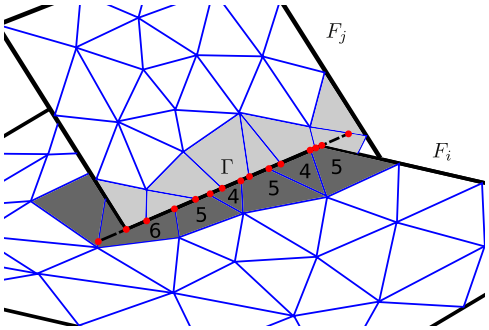

Fig. 1. Detail of the VEM conforming mesh at two intersecting fractures. (For interpretation of the references to color in this figure, the reader is referred to the web version of this article.)

3.1. Meshing process

Let $i \in \mathcal{I}$ be fixed and let us consider a generic fracture F_i in Ω with traces Γ_ℓ, $\ell \in \mathcal{L}_i$. The local mesh on the fracture is obtained starting from a regular triangular mesh, that is not required to be geometrically conforming with the traces. The triangular elements of this mesh that intersect the traces are then cut into polygons that do not cross the traces. This process is performed independently on each of the fractures in Ω, thus providing a polygonal mesh on each fracture that is locally conforming to the traces, i.e. with elements that do not cross any of the traces Γ_ℓ, $\ell \in \mathcal{L}_i$ of F_i, but instead cover them with edges of the triangulation. A globally conforming mesh of the whole network is finally obtained adding, on each trace Γ_ℓ on fracture F_i the vertexes on Γ_ℓ of the mesh of fractures F_j, with $i, j \in \mathcal{I}_\ell$: this increases the original number of edges of the mesh elements neighboring Γ_ℓ, forming polygons with flat angles at some vertexes. This discretization technique is the same proposed in [35] and exploits the flexibility of virtual elements in handling arbitrary polygonal elements. An example is proposed in Fig. 1, where two intersecting fractures are shown. The shadowed regions on both fractures represent the original triangles that are subsequently cut into polygons. The trace segment is prolonged up to meeting the first edge in the mesh and new polygons are created not crossing the prolonged segment. The numbers in some of the new elements on F_i represent the number of edges of the new polygonal mesh elements, whereas the red dots indicate mesh vertexes on the trace, shared by the two fractures. It can be noticed that in most cases a red dot corresponds to a polygon vertex with a flat angle.

After the generation of the globally conforming mesh, each trace Γ_ℓ, $\ell \in \mathcal{L}$ is split by mesh vertices into $n_e^{\Gamma_\ell}$ segments, each denoted by σ_t^ℓ, $t = 1, \ldots, n_e^{\Gamma_\ell}$. In order to ease the presentation of the method it is convenient to assume that to each segment σ_t^ℓ correspond two identical mesh edges on each fracture, thus having, in the global conforming mesh, a total of four copies of each trace edge, with their own outward unit normal vector. An example is shown in Fig. 2, where a generic fracture F_i in Ω is shown, with a single trace Γ_1 perpendicular to the

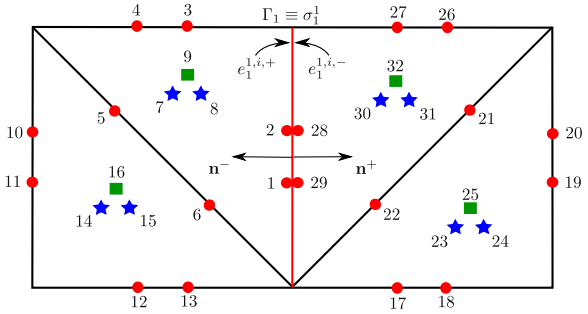

Fig. 2. Schematic of the mesh on a selected fracture with the degrees of freedom of the discrete spaces for Virtual Elements of order $k = 1$. (For interpretation of the references to color in this figure, the reader is referred to the web version of this article.)

horizontal boundary edges, and passing through their midpoints. As shown, the original trace segment $\sigma_1^1 \equiv \Gamma_1$ generates two mesh edges, $e_1^{1,i,+}$ and $e_1^{1,i,-}$ each endowed with an outward unit normal vector, $\mathbf{n}^+$, $\mathbf{n}^-$, with opposite direction.

Let us denote by $\mathcal{T}_{\delta,i}$ the mesh obtained in such a way on each fracture, $\mathcal{E}_{\delta,i}$ being the set of its edges, and we also set $\mathcal{T}_\delta = \cup_{\in I}\, \mathcal{T}_{\delta,i}$ and $\mathcal{E}_\delta = \cup_{i\in I}\, \mathcal{E}_{\delta,i}$. For each mesh element $E \in \mathcal{T}_\delta$, we set (x_E, y_E) to be the barycenter of E, and h_E to be the diameter of E.

3.2. Virtual spaces

Let $i \in I$ and $E \in \mathcal{T}_{\delta,i}$. The local VEM space for the velocity variable on each element E is

$$\begin{aligned}\mathbb{V}_{\delta,i}^E = \{&\mathbf{v}_\delta \in \mathrm{H(div,\,E)}\colon \mathbf{v}_\delta\cdot\mathbf{n}_e \in \mathbb{P}_k(\mathrm{e}) \quad \forall \mathrm{e}\in\partial\mathrm{E},\\ &\mathrm{div}(\mathbf{v}_\delta) \in \mathbb{P}_k(E),\ \text{ and } \mathrm{rot}(\mathbf{v}_\delta) \in \mathbb{P}_{k-1}(E)\},\end{aligned} \tag{9}$$

in which $\mathbb{P}_k(\omega)$ is the space of polynomials of maximum order k, and $e \subset \partial E$ is one of the edges of the boundary of E, and $\mathbf{n}_e$ is the unit outward normal vector to edge e. The condition on the rotor in (9) is required to fix the dimension of $\mathbb{V}_{\delta,i}^E$. The global discrete space on each element E is then:

$$\mathbb{V}_{\delta,i} := \{\mathbf{v}_\delta \in \mathbb{V}_i : \mathbf{v}_\delta|_E \in \mathbb{V}_{\delta,i}^E \quad \forall E \in \mathcal{T}_{\delta,i}\}. \tag{10}$$

We remark that functions in $\mathbb{V}_{\delta,i}$ have a continuous normal component in sub-fractures, whereas we have in general $[\![\mathbf{v}_{\delta,i}\cdot\mathbf{n}^i_{\Gamma_\ell}]\!] \neq 0$, $\forall\, \ell \in \mathcal{L}_i$. There are many choices for the degrees of freedom (DOFs) of functions in $\mathbb{V}_{\delta,i}$, see, e.g. [30,32,45]. In order to describe the DOFs used for the present work, let us introduce the following set of scaled monomials on each mesh element E, that span the space $\mathbb{P}_k(E)$ of dimension $n_k = (k+1)(k+2)/2$:

$$\mathbb{M}_k(E) = \left\{ m_\alpha(x,y) = \frac{(x-x_E)^{\alpha_1}(y-y_E)^{\alpha_2}}{h_E^{\alpha_1+\alpha_2}}, \quad |\alpha| = \alpha_1+\alpha_2 \le k \right\}.$$

Then let us introduce also the space

$$\nabla\mathbb{P}_{k+1}(E) := \{\mathbf{p} \in [\mathbb{P}_k(E)]^2 : \mathbf{p} = \nabla\hat{p} \text{ for some } \hat{p} \in \mathbb{P}_{k+1}(E)\}.$$

This space has dimension $n_{k+1} - 1$. Moreover, let $(\nabla\mathbb{P}_{k+1}(E))^\perp$ be the $\mathrm{L}^2(E)$ orthogonal complement of $\nabla\mathbb{P}_{k+1}(E)$ in $(\mathbb{P}_k(E))^2$, so that

$$(\mathbb{P}_k(E))^2 = (\nabla\mathbb{P}_{k+1}(E)) \oplus (\nabla\mathbb{P}_{k+1}(E))^\perp.$$

We remark that, in what follows, the space $(\nabla\mathbb{P}_{k+1}(E))^\perp$ could be replaced by any other space $(\nabla\mathbb{P}_{k+1}(E))^\star$ satisfying $(\nabla\mathbb{P}_{k+1}(E)) \oplus (\nabla\mathbb{P}_{k+1}(E))^\star = (\mathbb{P}_k(E))^2$. The space $(\nabla\mathbb{P}_{k+1}(E))^\perp$ is here used only for presentation purposes, whereas for the implementation of the method the choice described in [46] is used, which is computationally less expensive.

The dimension of the space $(\nabla\mathbb{P}_{k+1}(E))^\perp$ is

$$\begin{aligned}\dim[(\nabla\mathbb{P}_{k+1}(E))^\perp] &= \dim[(\mathbb{P}_k(E))^2] - \dim\,[\nabla\mathbb{P}_{k+1}(E)]\\ &= 2n_k - n_{k+1} + 1 = 2\frac{(k+1)(k+2)}{2} - \frac{(k+2)(k+3)}{2}\\ &= \frac{(k+2)(k-1)}{2} + 1,\end{aligned}$$

from which we deduce that $(\nabla\mathbb{P}_{k+1}(E))^\perp$ is not empty when $k \ge 1$. The space $\nabla\mathbb{P}_{k+1}(E)$ is spanned by

$$\nabla\mathbb{M}_{k+1}(E) := \{\mathbf{m} \in [\mathbb{M}_k(E)]^2 \colon \mathbf{m} = \nabla\widehat{m} \text{ for some } \widehat{m} \in \mathbb{M}_{k+1}(E),\ \widehat{m} \neq 1\},$$

whose orthogonal component in $[\mathbb{P}_k(E)]^2$ is denoted by $(\nabla\mathbb{M}_{k+1}(E))^\perp$.

As degrees of freedom on $\mathbb{V}_{\delta,i}^E$ we choose, $\forall\, \mathbf{v}_\delta \in \mathbb{V}_{\delta,i}$,

- the value of $\mathbf{v}_\delta\cdot\mathbf{n}_e$ at $k+1$ internal points on e, for each edge $e \subset \partial E$;
- if $k \ge 1$, the $n_k - 1$ products $(\mathbf{v}_\delta, \mathbf{m})_E$ for all $\mathbf{m} \in \nabla\mathbb{M}_k(E)$;
- if $k \ge 1$, the $(k+2)(k-1)/2 + 1$ products $(\mathbf{v}_\delta, \mathbf{m}^\perp)_E$ for all $\mathbf{m} \in (\nabla\mathbb{M}_{k+1}(E))^\perp$;

thus leading to the following number of degrees of freedom, n_{dof}^E for a polygonal element $E \in \mathcal{T}_\delta$ with $n_e{}^E$ vertices:

- if $k = 0$, $n_{\mathrm{dof}}^E = n_e{}^E$;
- if $k \ge 1$, $n_{\mathrm{dof}}^E = (k+1)n_e{}^E + k(k+2)$.

A schematic of the degrees of freedom for the discrete VEM space is reported in Fig. 2, in the case of a polynomial accuracy $k = 1$. According to the selected polynomial accuracy, two degrees of freedom are associated to each mesh edge and are marked with red dots and a consecutive numbering (the location of the DOFs in the picture is only indicative). Two DOFs are associated to each copy of the edge lying on the trace and we remark that this allows for a velocity solution with discontinuous normal component across the traces of each fracture. The set of DOFs for the velocity is completed by the two moments with respect to the monomials in $\nabla\mathbb{M}_1(E)$, denoted with a star shaped blue marker inside the element, and the moment with respect to $(\nabla\mathbb{M}_2(E))^\perp$, marked with green squares inside the element.

When building the global velocity space $\mathbb{V}_{\delta,i}$ on each fracture F_i, continuity of the normal component of $\mathbf{v}_\delta \in \mathbb{V}_{\delta,i}$ is enforced across each mesh element edge that does not lie on any of the traces Γ_ℓ, $\ell \in \mathcal{L}_i$, thus allowing jumps of the normal component of the velocity across fracture intersections both on each fracture and across intersecting fractures.

As in the case of the primal VEM formulation, the shape functions in the local VEM space are not explicitly known in general except for their DOFs, and thus computability of operators on the VEM functions is one of the key aspects in the VEM framework. Let us observe that the divergence of each VEM function can be exactly computed, by means of the set of DOFs. Indeed, since $\mathrm{div}(\mathbf{v}_\delta)|_E \in \mathbb{P}_k(E)$, we can exactly compute its components in the basis $\mathbb{M}_k(E)$ since, by Green's formula we have:

$$(\mathrm{div}(\mathbf{v}_\delta),\, m)_E = -\,(\mathbf{v}_\delta,\, \nabla m)_E + (\mathbf{v}_\delta\cdot\mathbf{n}_e,\, m)_{\partial E} \quad \forall m \in \mathbb{M}_k(E), \tag{11}$$

and the right-hand side is computable using the first two sets of degrees of freedom. Having computed $\mathrm{div}(\mathbf{v}_\delta)$, we can also compute the component-wise $\mathrm{L}^2(E)$-projection of $\mathbf{v}_\delta \in \mathbb{V}_{\delta i}^E$ on the space of polynomials of order k: $\Pi_k^0\colon \mathbb{V}_{\delta i}^E \to [\mathbb{P}_k(E)]^2$, defined by

$$(\Pi_k^0\mathbf{v}_\delta\mathbf{m})_E = (\mathbf{v}_\delta,\, \mathbf{m})_E \quad \forall \mathbf{m} \in [\mathbb{M}_k(E)]^2.$$

The right-hand side of this latter equation can be computed observing that, for any given $\mathbf{m} \in \mathbb{M}_k(E)$, we can decompose $\mathbf{m} = \mathbf{m}^\nabla + \mathbf{m}^\perp$, where $\mathbf{m}^\nabla \in \nabla\mathbb{M}_{k+1}(E)$ and $\mathbf{m}^\perp \in (\nabla\mathbb{M}_{k+1}(E))^\perp$. Let $\widehat{m} \in \mathbb{M}_{k+1}(E)$ be such that $\nabla\widehat{m} = \mathbf{m}^\nabla$; then

$$\begin{aligned}(\mathbf{v}_\delta,\, \mathbf{m})_E &= (\mathbf{v}_\delta,\, \mathbf{m}^\nabla)_E + (\mathbf{v}_\delta,\, \mathbf{m}^\perp)_E = (\mathbf{v}_\delta,\, \nabla\widehat{m})_E + (\mathbf{v}_\delta,\, \mathbf{m}^\perp)_E =\\ &= -\,(\mathrm{div}(\mathbf{v}_\delta),\, \widehat{m})_E + (\mathbf{v}_\delta\cdot\mathbf{n}_{\partial E},\, \widehat{m})_{\partial E} + (\mathbf{v}_\delta,\, \mathbf{m}^\perp)_E,\end{aligned}$$

and all terms on the last line are computable knowing $\mathrm{div}(\mathbf{v}_\delta)$ and the first and last set of degrees of freedom of $\mathbf{v}_\delta$.

Concerning the pressure variable, we define the set of DOFs on each mesh element E as the n_k moments with respect to the monomial basis $\mathbb{M}_k(E)$, and the global discrete space for the pressure is $\mathbb{Q}_\delta = \left\{ q_\delta\colon q_\delta|_{F_i} \in \mathbb{Q}_{\delta,i},\ \ i = 1,\ldots,N \right\}$, with

$$\mathbb{Q}_{\delta,i} := \left\{ q_\delta \in \mathrm{L}^2(F_i)\colon q_\delta|_E \in \mathbb{P}_k(E) \quad \forall E \in \mathcal{T}_{\delta,i} \right\}.$$

Note that no requirements of continuity are made for this space.

Let us now call $\mathcal{M}^\ell = \left\{ \mu_{\delta,\xi}^\ell,\ \xi = 1,\ldots,n_{\mathrm{dof}}^{\Gamma_\ell} \right\}$ the set of the degrees of freedom introduced on all the (duplicated) mesh edges $e \in \mathcal{E}_\delta$ lying on trace Γ_ℓ, $\ell \in \mathcal{L}$, and then let us set the space $\mathbb{G}_\delta$ as:

$$\mathbb{G}_\delta = \bigcup_{\ell\in\mathcal{L}} \mathcal{M}^\ell.$$

3.3. Mixed VEM discrete formulation

Let us fix $i \in \mathcal{I}$ and let us define

$a_{\delta i}$: $\mathbb{V}_{\delta,i} \times \mathbb{V}_{\delta,i} \to \mathbb{R}$, $\quad b_{\delta,i}$: $\mathbb{Q}_{\delta,i} \times \mathbb{V}_{\delta,i} \to \mathbb{R}$

such that, $\forall \mathbf{v}_\delta, \mathbf{w}_\delta \in \mathbb{V}_{\delta,i}$, $q_\delta \in \mathbb{Q}_{\delta,i}$:

$$a_{\delta,i}(\mathbf{w}_\delta, \mathbf{v}_\delta) := \sum_{E\in\mathcal{T}_{\delta,i}} (\nu\Pi_k^0\mathbf{w}_\delta, \Pi_k^0\mathbf{v}_\delta)_E + S^E((I-\Pi_k^0)\mathbf{w}_\delta, (I-\Pi_k^0)\mathbf{v}_\delta), \tag{12}$$

$$b_{\delta,i}(q_\delta, \mathbf{v}_\delta) := \sum_{E\in\mathcal{T}_{\delta,i}} (q_\delta, \beta\cdot\Pi_k^0\mathbf{v}_\delta)_E, \tag{13}$$

where S^E: $\mathbb{V}_{\delta,i} \times \mathbb{V}_{\delta,i} \to \mathbb{R}$ is a bilinear form such that $\forall\ \mathbf{v}_\delta \in \mathbb{V}_{\delta,i}$:

$$\exists\ \alpha_*, \alpha^* > 0\colon \alpha_* a_i^E(\mathbf{v}_\delta, \mathbf{v}_\delta) \le S^E(\mathbf{v}_\delta, \mathbf{v}_\delta) \le \alpha^* a_i^E(\mathbf{v}_\delta, \mathbf{v}_\delta) \quad \forall \mathbf{v}_\delta \in \ker\Pi_k^0,$$

in which $a_i^E(\cdot,\cdot)$ is the restriction of the bilinear form $a_i(\cdot,\cdot)$ to element $E \subset \mathcal{T}_{\delta,i}$. Then, setting $\forall\ \mathbf{v}_\delta, \mathbf{w}_\delta \in \mathbb{V}_\delta$, and $q_\delta \in \mathbb{Q}_\delta$

$$a_\delta(\mathbf{w}_\delta, \mathbf{v}_\delta) := \sum_{i\in\mathcal{I}} a_{\delta,i}\left(\mathbf{w}_\delta|_{F_i}, \mathbf{v}_\delta|_{F_i}\right), \quad b_\delta(q_\delta, \mathbf{v}_\delta) := \sum_{i\in\mathcal{I}} b_{\delta,i}\left(q_\delta|_{F_i}, \mathbf{v}_\delta|_{F_i}\right),$$

we write the following discrete problem: *find* $\mathbf{u}_{0\delta} \in \mathbb{V}_\delta$, $h_\delta \in \mathbb{Q}_\delta$, $\lambda_\delta \in \mathbb{G}_\delta$ such that:

$$\begin{cases} a_\delta(\mathbf{u}_{0\delta}, \mathbf{v}_\delta) - b_\delta(h_\delta, \mathbf{v}_\delta) - d(\mathbf{v}_\delta, h_\delta) + g(\lambda_\delta, \mathbf{v}_\delta) & \\ \qquad = -(h_{\delta D}, \mathbf{v}_\delta\cdot\mathbf{n})_{\Gamma_D} - a_\delta(\mathbf{u}_{\delta N}, \mathbf{v}_\delta) & \forall \mathbf{v}_\delta \in \mathbb{V}_\delta, \\ d(\mathbf{u}_{0\delta}, q_\delta) + c(h_\delta, q_\delta) = (f, q_\delta) - d(\mathbf{u}_{\delta N}, q_\delta) & \forall q_\delta \in \mathbb{Q}_\delta, \\ g(\mu_\delta, \mathbf{u}_{\delta 0}) = -g(\mu_\delta, \mathbf{u}_{\delta N}) & \forall \mu_\delta \in \mathbb{G}_\delta. \end{cases} \tag{14}$$

3.4. Well-posedness of the discrete problem

In order to prove the well posedness of (14), let us observe that according to the definition of the space $\mathbb{G}_\delta$ an inf-sup condition holds for the operator g: $\mathbb{G}_\delta \times \mathbb{V}_\delta \mapsto \mathbb{R}$. Indeed we have:

$$\forall\ \mu_\delta \in \mathbb{G}_\delta,\ \exists\ \mathbf{v}_\delta^* \in \mathbb{V}_\delta\colon \quad \frac{|g(\mu_\delta, \mathbf{v}_\delta^*)|}{\|\mathbf{v}_\delta^*\|_{\mathbb{V}_\delta}} = 1 \tag{15}$$

choosing $\mathbf{v}_\delta^*$ as the basis function of the VEM space corresponding to the degree of freedom μ_δ, and recalling that basis functions in $\mathbb{V}_\delta$ have discontinuous normal components across the traces on each fracture.

Then we place ourselves in the space $\mathcal{V}_\delta = \mathbb{V}_\delta \cap \ker(g)$, having the same local approximation properties of $\mathbb{V}_\delta$, and we re-write (14) as: *find* $\mathbf{u}_{0\delta} \in \mathcal{V}_\delta$, $h_\delta \in \mathbb{Q}_\delta$ *such that:*

$$\begin{cases} a_\delta(\mathbf{u}_{0\delta}, \mathbf{v}_\delta) - b_\delta(h_\delta, \mathbf{v}_\delta) - d(\mathbf{v}_\delta, h_\delta) & \\ \qquad = g(\mu_\delta, \mathbf{u}_{\delta N}) - (h_{\delta D}, \mathbf{v}_\delta\cdot\mathbf{n})_{\Gamma_D} - a_\delta(\mathbf{u}_{\delta N}, \mathbf{v}_\delta) & \forall \mathbf{v}_\delta \in \mathcal{V}_\delta, \\ d(\mathbf{u}_{0\delta}, q_\delta) + c(h_\delta, q_\delta) = (f, q_\delta) - d(\mathbf{u}_{\delta N}, q_\delta) & \forall q_\delta \in \mathbb{Q}_\delta, \end{cases}$$

whose well-posedness is proven in [32].

4. Implementation

This section is aimed at proving practical details of the algorithm, from the discretization strategy to the assembly of matrices that have to be computed.

For every fracture F_i, with $i \in \mathcal{I}$, let us denote by $n^v_{\mathrm{dof},i}$ the number of DOFs for the velocity space and $n^p_{\mathrm{dof},i}$ the number of DOFs for the pressure space on fracture F_i and let $n_{\mathrm{dof},i} := n^v_{\mathrm{dof},i} + n^p_{\mathrm{dof},i}$. It is also $n^v_{\mathrm{dof}} = \sum_{i\in\mathcal{I}} n^v_{\mathrm{dof},i}$ and $n^p_{\mathrm{dof}} = \sum_{i\in\mathcal{I}} n^p_{\mathrm{dof},i}$ defined as the total number of DOFs throughout the whole network for the velocity and pressure spaces, respectively. We collect the degrees of freedom for the velocity space in a vector $\overline{\mathbf{u}} \in \mathbb{R}^{n^v_{\mathrm{dof}}}$, and the degrees of freedom for the pressure in a vector $\overline{\mathbf{h}} \in \mathbb{R}^{n^p_{\mathrm{dof}}}$.

Let us introduce matrix $A_i \in \mathbb{R}^{n^v_{\mathrm{dof},i}\times n^v_{\mathrm{dof},i}}$ defined as

$$(A_i)_{jk} = a_{\delta i}(\boldsymbol{\varphi}_{i,k}, \boldsymbol{\varphi}_{i,j})$$

representing the discrete operator $a_{\delta,i}$ on each fracture F_i, $i = 1,\ldots,N$, defined as in (12), and in which $\boldsymbol{\varphi}_{i,j}$, $j = 1,\ldots, n^i_{\mathrm{dof},i}$ are the VEM basis functions of the finite-dimensional discrete space $\mathbb{V}_{\delta,i}$ for the velocity on F_i. The computation of the projection operator is as in (11), whereas the stabilization term $S^E(\mathbf{v}_\delta, \mathbf{w}_\delta)$, for $\mathbf{v}_\delta, \mathbf{w}_\delta \in \mathbb{V}_{\delta,i}$ is defined as the euclidean scalar product of the degrees of freedom of $\mathbf{v}_\delta$, $\mathbf{w}_\delta$ multiplied by a factor $\nu^E := h_E^2\nu(x_E, y_E)$. Furthermore, being $\chi_{i,k} \in \mathbb{Q}_{\delta,i}$, for $k = 1,\ldots, n^p_{\mathrm{dof},i}$, the basis functions of the finite-dimensional space for the pressure variable on F_i, we denote by:

$$(B_i)_{jk} = b_{\delta,i}\left(\varphi_{i,k}, \chi_{i,j}\right) \quad (C_i)_{jk} = c_i\left(\chi_{i,k}, \chi_{i,j}\right) \quad (D_i)_{jk} = d_i\left(\varphi_{i,k}, \chi_{i,j}\right)$$

the matrices associated with the bilinear forms $b_{\delta,i}$ in (13), c_i in (5) and d_i in (6), respectively. It is then possible to write an independent saddle point problem on each fracture F_i of the network, expressing the advection diffusion problem on each fracture and corresponding to the first two equations in (14). The structure of the saddle point matrix $K_i \in \mathbb{R}^{n_{\mathrm{dof},i}\times n_{\mathrm{dof},i}}$, $i \in \mathcal{I}$ is:

$$K_i = \begin{bmatrix} A_i & -B_i - D_i \\ D_i^\top & C_i \end{bmatrix}. \tag{16}$$

We then construct column vectors $\mathbf{f}_i \in \mathbb{R}^{n_{\mathrm{dof},i}}$, $i \in \mathcal{I}$, as the vector of load values and boundary condition terms. Assembling matrices on the whole DFN we have:

$$K = \begin{bmatrix} K_1 & 0 & \cdots & 0 \\ 0 & K_2 & \cdots & \vdots \\ \vdots & \vdots & \ddots & \vdots \\ 0 & \cdots & \cdots & K_N \end{bmatrix} \text{ and } \mathbf{f} = \begin{bmatrix} \mathbf{f}_1 \\ \vdots \\ \vdots \\ \mathbf{f}_N \end{bmatrix}.$$

We remark that matrices K_i are singular for fractures F_i, $i \in \mathcal{I}$ with pure Neumann boundary conditions, the uniqueness of the solution deriving from the matching among all the fractures on the network, which is given by the last equation in (14), not yet enforced here.

To this end, let us recall that each trace Γ_ℓ, $\ell \in \mathcal{L}$ is given by the union of segments σ_t^ℓ, $t = 1,\ldots, n_e^{\Gamma_\ell}$. To each segment σ_t^ℓ of Γ_ℓ four mesh edges are associated, denoted by $\{e_t^{\ell,i,+}, e_t^{\ell,i,-}, e_t^{\ell,j,+}, e_t^{\ell,j,-}\} := \mathcal{E}_{\delta,t}^\ell \subset \mathcal{E}_\delta$, with $i, j \in \mathcal{I}_\ell$ and the $+$ or $-$ sign is chosen depending if the mesh edge belongs to the element on the right or left side of σ_t^ℓ, respectively, after fixing an orientation for σ_t^ℓ on F_i and F_j, independently. On a trace Γ_ℓ, for a given polynomial accuracy k, we associate $k+1$ DOFs to each edge $e_t^{\ell,i,\star} \in \mathcal{E}_{\delta,t}^\ell$, with $\star$=+ or $-$ and we denote by $u_{t,\xi}^{\ell,i,\star}$, $\xi = 1,\ldots, k+1$ each of these DOFs. It is possible to introduce a function κ, such that, for $\ell \in \mathcal{L}$, $i \in \mathcal{I}_\ell$, $\star \in \{+,-\}$, $t = 1,\ldots, n_e^{\Gamma_\ell}$, and $\xi = 1,\ldots, k+1$, the number $\kappa(\ell, t, \xi, i, \star) \subset 1,\ldots, n^v_{\mathrm{dof}}$ corresponds to the index of the degree of freedom $u_{t,\xi}^{\ell,i,\star}$ in the global numbering. For each trace Γ_ℓ, for each $t = 1,\ldots, n_e^{\Gamma_\ell}$ it is possible to write $k+1$ conditions enforcing the balance of the normal component of the velocity at fracture intersections, by simply setting to zero the sum of the basis functions on the edges in $\mathcal{E}_{\delta,t}^\ell$ as follows: for $\xi = 1, \ldots, k+1$:

$$\Lambda_{\ell,t,\xi}\overline{\mathbf{u}} = 0,$$

being $\Lambda_{\ell,t,\xi} \in \mathbb{R}^{n^v_{\mathrm{dof}}}$ defined as:

$$\Lambda_{\ell,t,\xi} := \begin{matrix} \kappa_1 & & \kappa_2 & & \kappa_3 & & \kappa_4 \end{matrix}$$
$$\begin{pmatrix} 0 & \cdots & 1 & \cdots & 1 & \cdots & 1 & \cdots & 1 & \cdots 0 \end{pmatrix}$$

and, for $i, j \in \mathcal{I}_\ell$, $(\kappa_\mathfrak{q})_{\mathfrak{q}=1,\ldots,4}$ is the ordered set of the values:

$$\{\kappa(\ell,t,\xi,i,+),\ \kappa(\ell,t,\xi,i,-),\ \kappa(\ell,t,\xi,j,+),\ \kappa(\ell,t,\xi,j,-)\}.$$

Then it is possible to collect column-wise row vectors $\Lambda_{\ell,t,\xi}$ for $\ell \in \mathcal{L}$, $t = 1,\ldots, n_e^{\Gamma_\ell}$, and $\xi = 1,\ldots, k+1$ as to form matrix $\Lambda \in \mathbb{R}^{((k+1)\sum_{\ell\in\mathcal{L}} n_e^{\Gamma_\ell})\times n^v_{\mathrm{dof}}}$, and then matrix $\mathfrak{L} = [\Lambda, \mathbf{0}_p]$, with $\mathbf{0}_p \in \mathbb{R}^{n^p_{\mathrm{dof}}\times n^p_{\mathrm{dof}}}$ being the null matrix. Finally, if we let λ be the vector of values of the Lagrange multipliers of the system, and setting $\mathbf{s} = [\overline{\mathbf{u}}^\top, \overline{\mathbf{h}}^\top]^\top$ we have that the final linear system corresponding to the

discrete problem (14) is:

$$\begin{bmatrix} K & \mathfrak{L}^T \\ \mathfrak{L} & O \end{bmatrix} \begin{bmatrix} \mathbf{s} \\ \boldsymbol{\lambda} \end{bmatrix} = \begin{bmatrix} \mathbf{f} \\ \mathbf{0} \end{bmatrix}. \tag{17}$$

This type of system is in the standard form that arises when applying domain decomposition methods. We refer the reader to [47–50].

5. Numerical results

Let us now show some numerical tests performed on networks of increasing complexity. Approximation spaces with polynomial accuracy up to order $k = 5$ are considered: the mixed discrete VEM space is used for the space of the velocity and the space of element-wise polynomials of the same order is used for the pressure space.

The first two considered problems take into account simple networks of up to three fractures, for which an analytic solution is known, and convergence curves are presented to compare the obtained convergence rates with the optimal ones reported in [32]. Subsequently some simulations on more complex DFNs are proposed, aimed at showing the applicability of the method, and also to provide some qualitative insight on the behaviour of the method.

5.1. Benchmark problems

As a first example, a 3 fracture, 3 trace network is analyzed, labeled BP1. The domain is the same as the one in [35], and is shown in Fig. 3. Here an advection-diffusion-reaction problem is considered, with non constant coefficients and it is solved in mixed formulation.

The computational domain Ω is given by the union of fractures F_1, F_2 and F_3, defined as follows:

$$\begin{aligned} F_1 &= \{(x, y, z) \in \mathbb{R}^3 : -1 \le x \le 1,\ -1 \le y \le 1,\ z = 0\}, \\ F_2 &= \{(x, y, z) \in \mathbb{R}^3 : -1 \le y \le 1,\ -1 \le z \le 1,\ x = 0\}, \\ F_3 &= \{(x, y, z) \in \mathbb{R}^3 : -1 \le z \le 0,\ -1 \le x \le 1,\ y = 0\}, \end{aligned}$$

with three intersections:

$$\begin{aligned} \Gamma_1 &= \{(x, y, z) \in \mathbb{R}^3 : -1 \le x \le 1,\ y = 0,\ z = 0\}, \\ \Gamma_2 &= \{(x, y, z) \in \mathbb{R}^3 : -1 \le y \le 1,\ z = 0,\ x = 0\}, \\ \Gamma_3 &= \{(x, y, z) \in \mathbb{R}^3 : -1 \le z \le 0,\ x = 0,\ y = 0\}. \end{aligned}$$

Introducing a fracture-local reference system $(\hat{x}, \hat{y})$ we define, on each fracture F_i, $i = 1, \ldots, 3$:

$$\begin{aligned} \mathrm{K}_i(\hat{x}, \hat{y}) &= \begin{pmatrix} 1 + \hat{y}^2 & -\hat{x}\hat{y}/2 \\ -\hat{x}\hat{y}/2 & 1 + \hat{x}^2 \end{pmatrix}, \\ \mathbf{b}_i(\hat{x}, \hat{y}) &= (\hat{x} - \hat{y}, \hat{y} - 1), \\ \gamma_i(\hat{x}, \hat{y}) &= \hat{x}^3 + \hat{y}, \end{aligned}$$

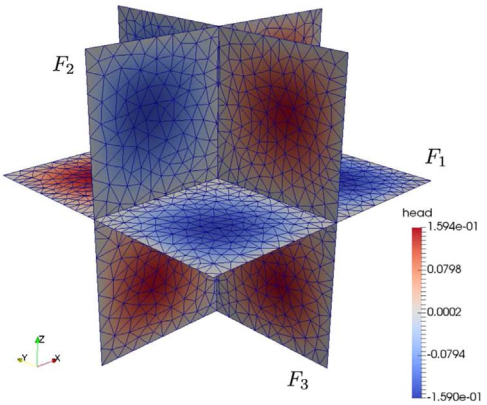

Fig. 3. BP1: spatial distribution of fractures.

and the problem is formulated as in (1), being the load terms f_i, $i = 1, \ldots, 3$ such that the exact solution on each fracture is:

$$\begin{aligned} h_1(x, y) &= |x|(1 + x)(1 - x)y(1 + y)(1 - y), \\ h_2(y, z) &= y(1 + y)(1 - y)|z|(1 + z)(1 - z), \\ h_3(z, x) &= z(1 + z)(1 - z)x(1 + x)(1 - x), \end{aligned}$$

which is shown in Fig. 3 interpolated on an example mesh, with coloring proportional to the hydraulic head values. The problem is solved on meshes with a number of degrees of freedom ranging from about 1×10^2 to about 6×10^4 and the following error norms are considered to evaluate accuracy of the numerical solution:

$$h_{\mathrm{err}} = \left(\sum_{E \in \mathcal{T}_\delta} \|h - h_\delta\|_E^2 \right)^{\frac{1}{2}},$$

$$\mathbf{u}_{\mathrm{err}} = \left(\sum_{E \in \mathcal{T}_\delta} \|\mathbf{u} - \Pi_k^0 \mathbf{u}_\delta\|_E^2 \right)^{\frac{1}{2}},$$

$$(\nabla \cdot \mathbf{u})_{\mathrm{err}} = \left(\sum_{E \in \mathcal{T}_\delta} \|\nabla \cdot (\mathbf{u} - \mathbf{u}_\delta)\|_E^2 \right)^{\frac{1}{2}}.$$

Fig. 4 shows convergence rates of the above quantities against the number of DOFs when the computational mesh is refined. The various considered polynomial accuracy orders, ranging from $k = 0$ to $k = 5$ are reported in different plots. In all cases the expected convergence rates are obtained, with some instances of superconvergence for the pressure variable for coarser meshes. Fig. 5 displays, instead, convergence curves of h_{err}, $\mathbf{u}_{\mathrm{err}}$ and $(\nabla \cdot \mathbf{u})_{\mathrm{err}}$ against DOF numbers when the polynomial accuracy order is increased from $k = 0$ to $k = 5$. Four different fixed geometrical meshes are reported. In all cases it is possible to observe exponential convergence rates.

The second benchmark problem, labeled BP2, revisits a 2 fracture DFN, also studied in [35]. This problem is interesting as it allows us to test the method when applied to geometrical configurations with the presence of a trace ending in the interior of some fracture, which causes a loss of regularity in the solution, also away from the traces. The computational domain $\Omega = F_1 \cup F_2$ is displayed in Fig. 6, and the two fractures, F_1 and F_2 are defined as:

$$\begin{aligned} F_1 &= \{(x, y, z) \in \mathbb{R}^3 : -1 \le x \le 1,\ -1 \le y \le 1,\ z = 0\}, \\ F_2 &= \{(x, y, z) \in \mathbb{R}^3 : -1 \le x \le 0,\ -1 \le z \le 1,\ y = 0\}, \end{aligned}$$

intersecting in the trace $\Gamma = \{(x, y, z) \in \mathbb{R}^3 : y = 0, z = 0 \text{ and } -1 \le x \le 0\}$, whose tip is in the interior of F_1.

The problem is as follows:

$$\begin{cases} -\Delta h = f_1 & \text{in } F_1 \backslash \Gamma, \\ -\Delta h = f_2 & \text{in } F_2 \backslash \Gamma, \\ h = 0 & \text{on } \partial\Omega \backslash \Gamma_D^*, \\ h = (z^2 - z^4)\cos(\pi/4) & \text{on } \Gamma_D^*, \end{cases}$$

being Γ_D^* the portion of the boundary of Ω with a non-null Dirichlet boundary condition, as shown in Fig. 6. The forcing terms f_i, $i = 1,2$ are such that the exact solution for this problem is:

$$h_1(x, y, z) = -\cos\left(\frac{1}{2}\mathrm{arctan2}(x, y)\right)(x^2 - 1)(y^2 - 1)(x^2 + y^2),$$

$$h_2(x, y, z) = \cos\left(\frac{1}{2}\mathrm{arctan2}(z, x)\right)(z^2 - 1)(x^2 - 1)(z^2 + x^2),$$

where $\mathrm{arctan2}(x, y)$ is the inverse tangent function with 2 arguments, that returns the appropriate quadrant of the angle whose tangent is y/x. We remark that the regularity of the solution is such that $h_1 \in \mathrm{H}^2(F_1 \backslash \Gamma)$ but $h_1 \notin \mathrm{H}^3(F_1 \backslash \Gamma)$. The exact solution is reported in Fig. 6, where the coloring is proportional to the hydraulic head, and an example mesh is also shown. The computed numerical solution h_δ is reported in

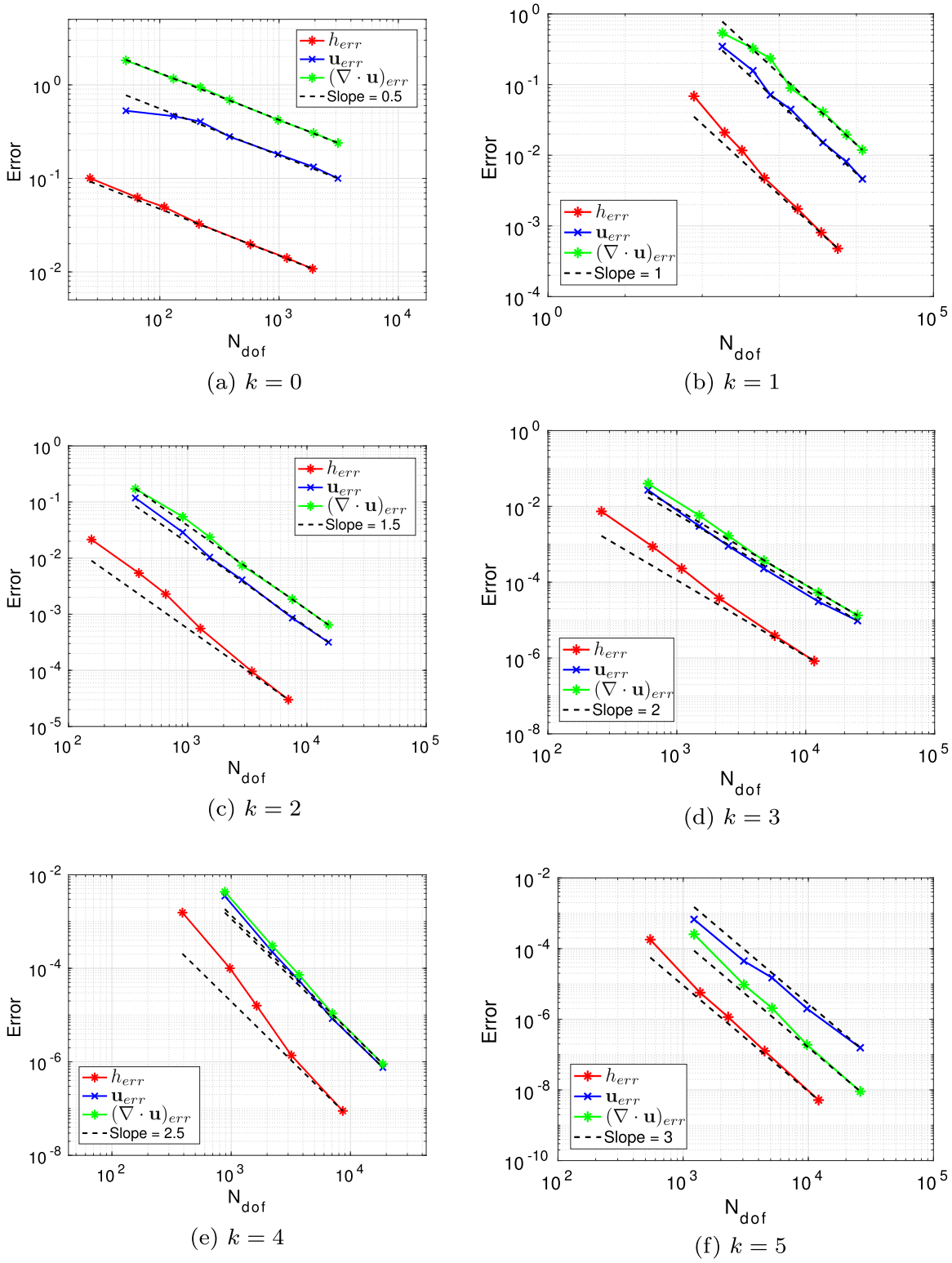

(a) $k = 0$ (b) $k = 1$ (c) $k = 2$ (d) $k = 3$ (e) $k = 4$ (f) $k = 5$

Fig. 4. BP1: convergence curves of the computed error norms against the number of DOFs at refining the mesh.

Fig. 7(a)-(b) for orders of polynomial accuracy $k = 0$ and $k = 2$, respectively, on fracture F_1. A finer mesh is used for the lower order approximation in order to have a similar number of DOFs for the two reported solutions (3109 and 3071 DOFs respectively).

Convergence rates against DOFs for approximation spaces of polynomial accuracy of orders from 0 to 5 are shown in Table 1, whereas convergence curves for the error norms h_{err}, $\mathbf{u}_{\text{err}}$ and $(\nabla \cdot \mathbf{u})_{\text{err}}$ against DOF numbers for increasing polynomial order $k = 0, \ldots, 5$ are displayed in Fig. 8, for four different fixed polygonal meshes. As expected, given the low regularity of the solution, convergence rates for the error in the pressure variable does not improve increasing the accuracy of the approximation space from order 2 onward, whereas the convergence rates concerning the velocity field and its divergence do not improve from approximation orders $k = 1$ and $k = 0$ onward,

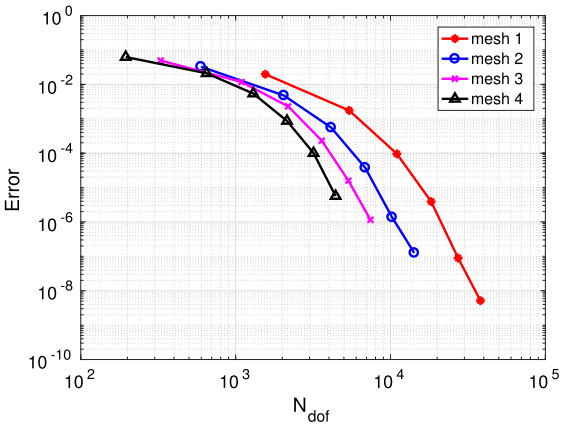

(a) h_{err}

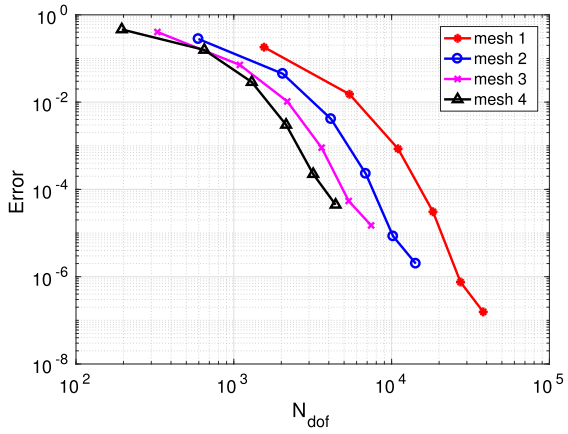

(b) $\mathbf{u}_{\mathrm{err}}$

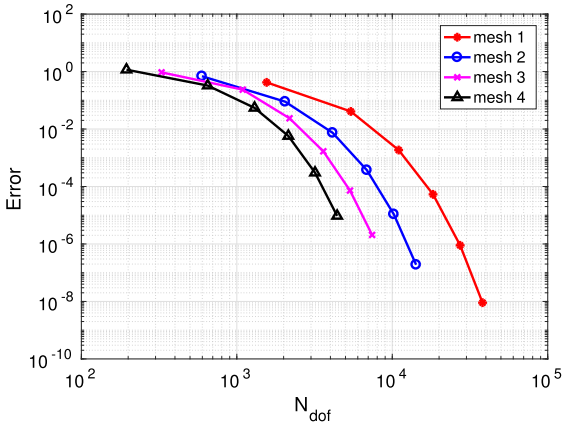

(c) $(\nabla \cdot \mathbf{u})_{\mathbf{err}}$

Fig. 5. BP1: convergence curves of the computed error norms against the number of DOFs at increasing values of the polynomial accuracy on four meshes.

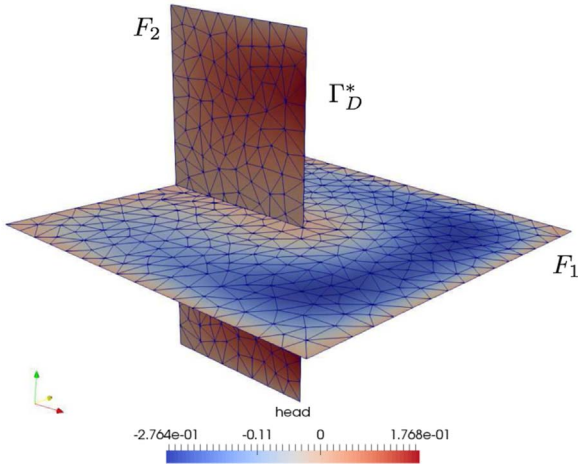

Fig. 6. BP2: spatial distribution of fractures.

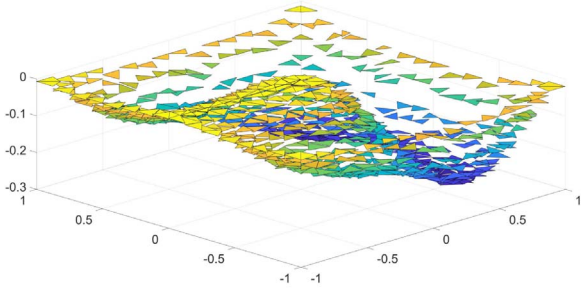

(a) $k = 0$

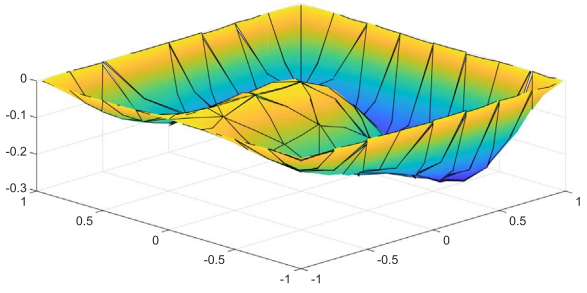

(b) $k = 2$

Fig. 7. BP2: discrete solutions for fracture 1 and orders $k = 0$ and $k = 2$ on two different geometrical meshes with approximately the same number of DOFs.

respectively. It can be noticed that in practical DFN configurations, a high regularity of the solution should not be expected due to the presence of traces ending in the interior of the fractures.

5.2. DFN simulations

This subsection is devoted to the description of results obtained applying the method to the study of bigger networks. Throughout this

Table 1
BP2: experimental convergence rates against DOF number.

Order	h_{err}	$\mathbf{u}_{\text{err}}$	$(\nabla\cdot\mathbf{u})_{\text{err}}$
0	0.5210	0.5144	0.5015
1	1.0376	0.9989	0.6021
2	1.5171	1.1006	0.5135
3	1.5540	1.1569	0.5550
4	1.4054	1.1267	0.5329
5	1.4794	1.1592	0.4907

subsection a maximum level of polynomial accuracy $k = 2$ is used. At first, a small-sized 6 fracture and 6 trace DFN is considered, labeled DFN6. Despite its simplicity, it serves to give a clear description on how the method performs, and the insight it provides can be easily carried over to more complex problems. The geometrical domain Ω for this experiment is shown in Fig. 9, along with an example computed solution in which the grading colors are proportional to hydraulic head values. The Laplace problem in mixed form is solved in Ω and, with reference to Fig. 9, a unitary Neumann boundary condition is imposed on the edge marked with Γ_{N1} on F_1 (also called source fracture), whereas a zero Dirichlet boundary condition is imposed on the edge marked by Γ_{D5} on F_5 (the sink fracture). All other fracture edges are insulated. Three different meshes are considered, as detailed in Table 2, in which the mesh parameter δ corresponds to the maximum element diameter of the original triangular mesh.

The results reported in Figs. 10–12 are obtained on the finest mesh considered. Fig. 10 displays the velocity field on fracture F_2 for a solution with a polynomial accuracy $k = 1$; the velocity fields obtained for values of $k = 0$ and $k = 2$ are practically indistinguishable. Fracture

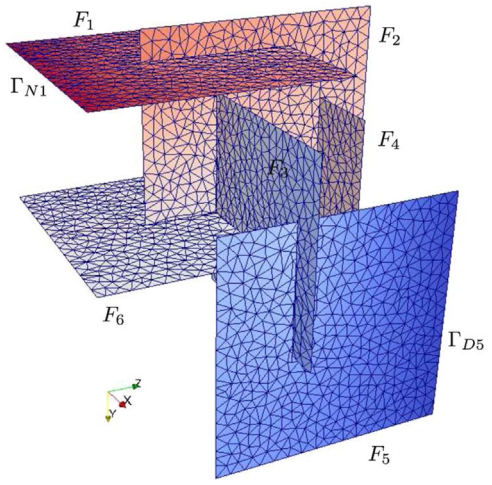

Fig. 9. DFN6: spatial geometry with source(F_1) and sink (F_5) fracture.

Table 2
DFN6: number of DOFs for the considered mesh parameters δ and polynomial accuracy levels k.

Order	Mesh		
	$\delta = 1.09$	$\delta = 0.70$	$\delta = 0.26$
0	975	2039	8458
1	3190	6798	29,304
2	6335	13,597	59,441

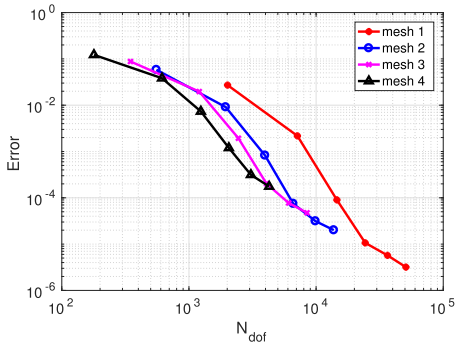

(a) h_{err}

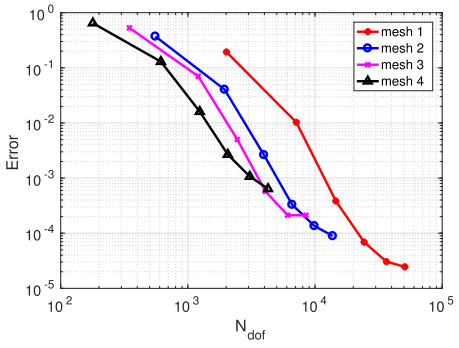

(b) $\mathbf{u}_{\text{err}}$

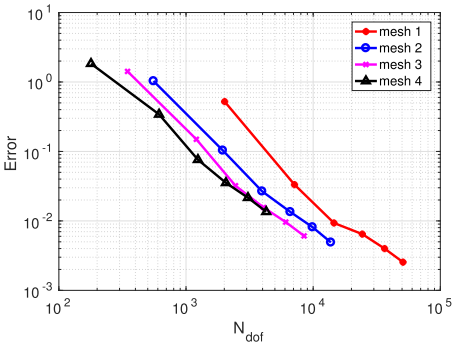

(c) $(\nabla \cdot \mathbf{u})_{\mathbf{err}}$

Fig. 8. BP2: convergence curves of the computed error norms against the number of DOFs at increasing values of the polynomial accuracy on four meshes.

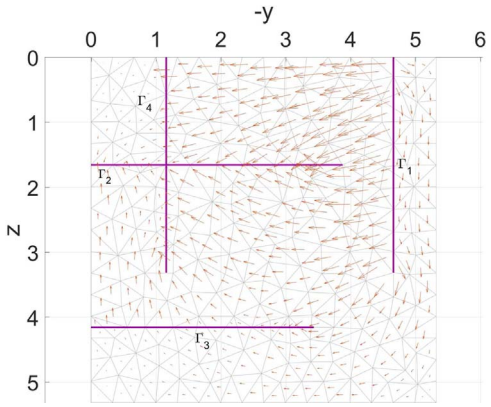

Fig. 10. DFN6: velocity field on fracture F_2, $\delta = 0.26$, $k = 1$.

F_2 has four traces Γ_ℓ, $\ell = 1, \ldots, 4$ given by the intersections of F_2 with fractures F_1, F_3, F_4 and F_6, respectively. As expected, flow enters F_2 through trace Γ_1 that is shared by F_2 and the source fracture, and leaves the fracture through traces Γ_2 and Γ_4. Trace Γ_3 connects F_2 to F_4, which is an insulated fracture: indeed it can be seen that there is both flux entering trace Γ_4 and leaving it, with a net balance of zero flux (see the following Table 4). Figs. 11(a)-(c) show the solution h_δ on fracture F_2 for the three different polynomial accuracy values. It can be noticed that pressure head values are quite similar among the three pictures and, even though there is no condition for pressure head continuity imposed by problem formulation (the functions in the pressure space are discontinuous across mesh elements), the solutions for orders 1 and 2 nevertheless exhibit a practically continuous behavior.

We introduce a quantity Δ_h defined as:

$$\Delta_h^2 = \frac{1}{L^2} \sum_{\ell \in \mathcal{L}} \| h_{\mathrm{av},i,\ell} - h_{\mathrm{av},j,\ell} \|_0^2$$

with $i, j \in \mathcal{I}_\ell$, and L is the number of traces in the network. The quantity $h_{\mathrm{av},i,\ell}$ is the average of the discrete pressure on the two sides of trace Γ_ℓ on fracture F_i, for $i \in \mathcal{I}$, $\ell \in \mathcal{L}_i$, and thus Δ_h is a measure of how discontinuous the pressure head is in the obtained solution across the traces, averaged by the number of traces. Since the discrete solution is discontinuous across each mesh edge, it is not possible to attain a zero value for Δ_h, but it is expected that its value decreases when the approximation space is increased. The obtained values of Δ_h are shown in Table 3 for the various meshes and the different orders of accuracy k. It can be seen that, as expected, the quantity Δ_h decreases both when the mesh is refined and when the order of polynomial accuracy is increased, showing a desired converging behavior towards a solution that is continuous at the traces.

In Fig. 12 the flux along trace $\Gamma_4 = F_2 \cap F_6$ is presented for the finest mesh ($\delta = 0.26$), with a comparison among the different accuracy

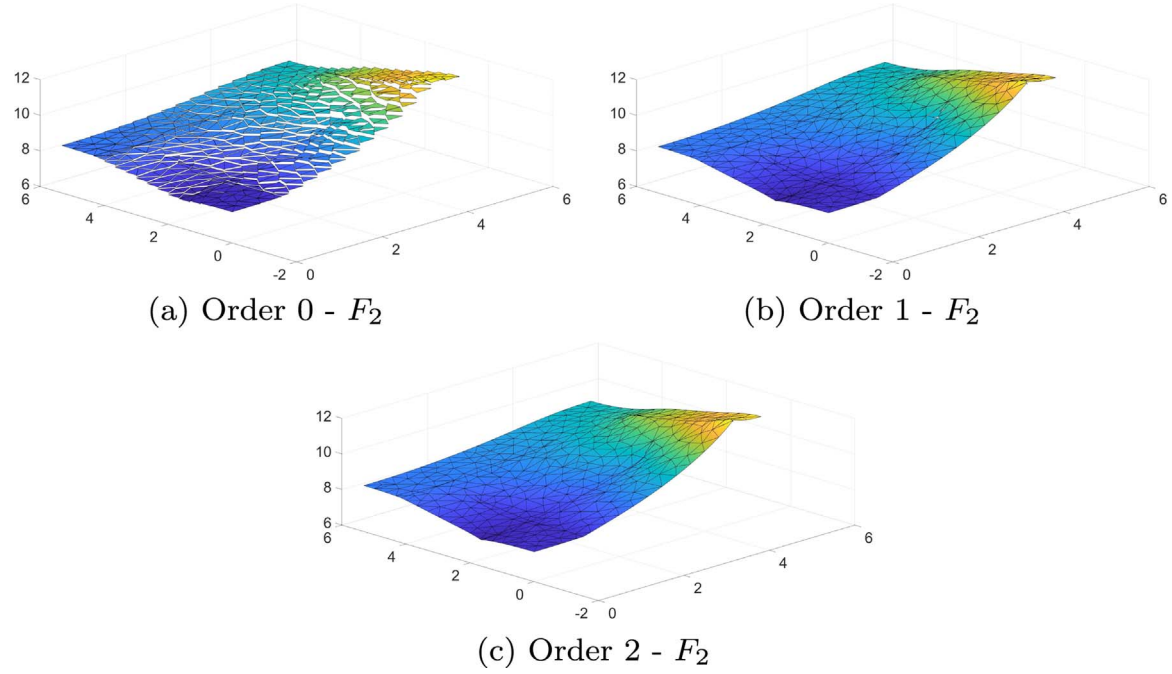

Fig. 11. DFN6: solution h_δ on fracture F_2 for orders 0 to 2, $\delta = 0.26$.

Table 3
DFN6: values of Δ_h for the various considered meshes and polynomial accuracy orders.

Order	Mesh		
	$\delta = 1.09$	$\delta = 0.70$	$\delta = 0.26$
0	5.2×10^{-1}	2.9×10^{-1}	1.1×10^{-1}
1	1.4×10^{-1}	9.4×10^{-2}	2.5×10^{-2}
2	9.5×10^{-2}	5.5×10^{-2}	1.4×10^{-2}

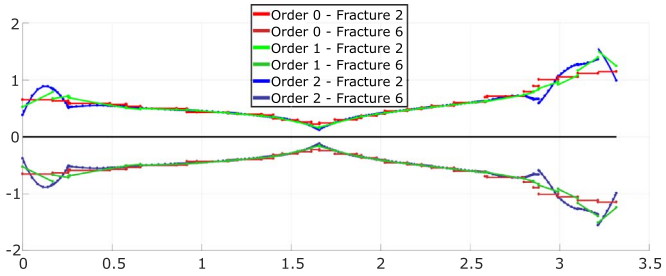

Fig. 12. DFN6: normal velocity on the trace Γ_4 for orders 0 to 2, $\delta = 0.26$.

Table 4
DFN6: flux data and flux mismatches across traces (last column) and flux balance on fractures (last row) for order $k = 0$, $\delta = 0.26$.

	F_1	F_2	F_3	F_4	F_5	F_6	Balance
Γ_1	−5.3174	5.3174	0	0	0	0	0
Γ_2	0	−3.4141	3.4141	0	0	0	0
Γ_3	0	6.5e−12	0	−6.5e−12	0	0	−6.9e−17
Γ_4	0	−1.9032	0	0	0	1.9032	−4.4e−16
Γ_5	0	0	−5.3174	0	5.3174	0	8.9e−16
Γ_6	0	0	1.9032	0	0	−1.9032	0
Balance	−5.3174	4.7e-10	4.4e−16	−6.5e-12	5.3174	1.7e-11	4.4e-16

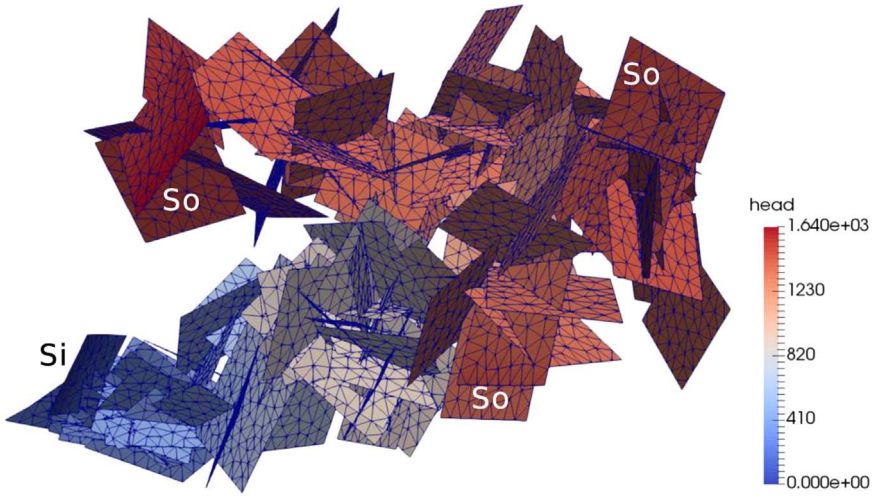

Fig. 13. DFN134: spatial geometry.

orders. In all cases the approximations are similar and, as expected, second order elements are able to better reproduce details in the flux function, such as larger variations over small distances, while lower order elements are capable at capturing the mean value of the flux exchange. Practically the same net flux is obtained when integrating the complete profile in all cases.

Table 4 details the flux exchange in fractures and traces for the finest considered mesh and a polynomial accuracy $k = 0$: rows correspond to traces, whereas columns to fractures. The last row contains the sum of all the incoming and outgoing flux for each fracture, while the last column shows, for each trace, the balance in flux exchange between the two fractures that share the trace. An almost exact flux balance is obtained, both within fractures and in trace exchanges, for all orders of accuracy. The incoming flux from fracture F_1 is perfectly balanced with the outgoing flux in F_5: fracture F_1 acts as a source that provides a total flux of 5.3174 to the system from the Neumann edge (negative values represent flux leaving the fracture through the traces), which leaves the system at fracture F_5 with a practical 0 unbalance reported in the bottom-right cell of the table. All other fractures show an almost null net flow, which agrees with the homogeneous Neumann boundary condition. As already mentioned, the flux exchange in trace T_3 is almost zero since fracture F_4 is neither a source nor a sink fracture and since it has only one intersection with another fracture (F_2).

According to the previous analysis it can be concluded that the mixed formulation shows a very high accuracy when computing flux exchange between fractures. The flux balance is almost exact for any order of accuracy of the method. Low order elements also show a very good performance with much less computational demand.

The last proposed example considers a larger network consisting of 134 fractures and 604 traces that more closely resembles a real network. This problem is labeled DFN134 and its geometry is shown in Fig. 13. In this network there is a wider range of fracture sizes and it has fractures intersecting at varying angles that originate several geometrical difficulties such as almost parallel and very close traces, small angles, small edges and badly shaped elements. Boundary conditions are imposed, with a homogeneous Dirichlet boundary condition on one edge of a sink fracture (labeled *Si* in the picture) and three prescribed incoming flux values of 100, 200 and 200 on one edge of three different source fractures (*So* in the picture). The Laplace problem is solved in mixed form with approximation spaces of orders 0, 1 and 2 on four different meshes, as detailed in Table 5.

An example solution on the whole network is shown in Fig. 13, in which the coloring is proportional to h_δ values. In Fig. 14 results for h_δ and orders $k = 0, 1, 2$ for a selected fracture are presented on the mesh with $\delta = 3.68$, whereas the velocity field is shown in Fig. 15 on the same mesh and a order $k = 2$. There are 18 traces present in the fracture generating a complex geometry that nevertheless is handled smoothly by the Virtual Element discretization. In Table 6 the quantity Δ_h is reported for the various meshes and orders of accuracy considered, showing again a clear convergent trend towards a solution continuous at the traces, when either the mesh is refined or the polynomial accuracy is increased. In Table 7 results for flux balance are presented, on the mesh with $\delta = 3.68$

Table 5
DFN134: Number of DOFs for the considered meshes and polynomial accuracy values.

Order	Mesh			
	$\delta = 11.34$	$\delta = 8.09$	$\delta = 5.95$	$\delta = 3.68$
0	43,630	53,080	65,149	98,353
1	125,020	153,764	190,742	295,594
2	234,730	290,151	361,668	567,001

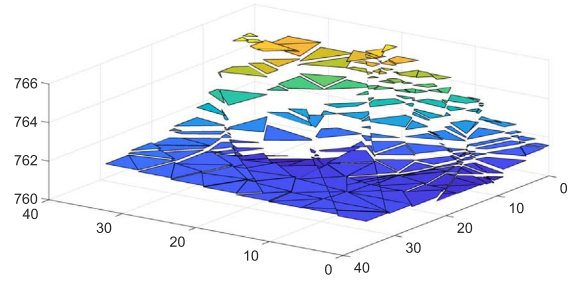

(a) Order 0 - Pressure head

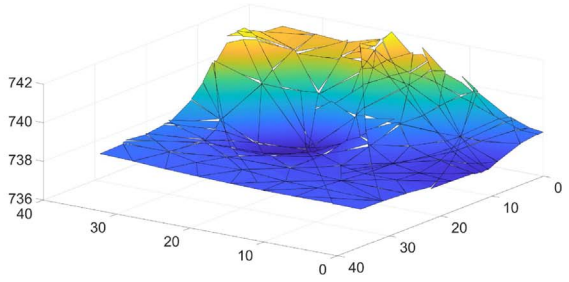

(b) Order 1 - Pressure head

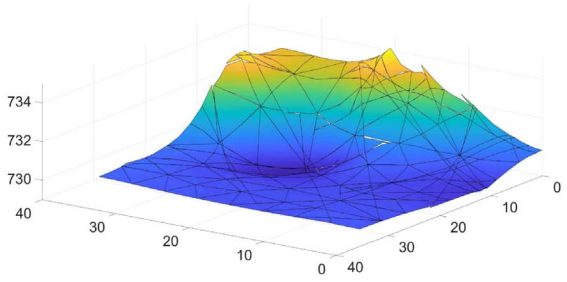

(c) Order 2 - Pressure head

Fig. 14. DFN134: solution h_δ for a selected fracture for different various of polynomial accuracy and $\delta = 3.68$.

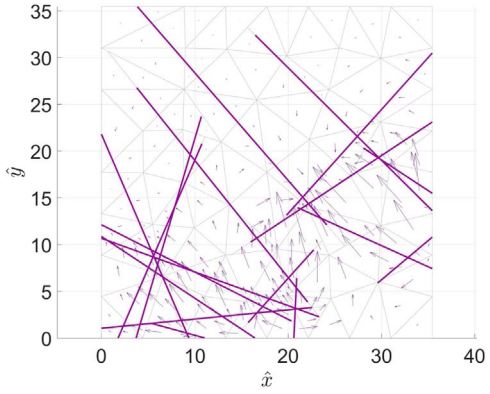

Fig. 15. DFN134: velocity field for the 134 fracture network on a selected fracture with order 2, $\delta = 3.68$.

Table 6
DFN134: values of Δ_h for the various considered meshes and polynomial accuracy orders.

Order	Mesh			
	$\delta = 11.34$	$\delta = 8.09$	$\delta = 5.95$	$\delta = 3.68$
0	1.81	1.44	1.15	0.83
1	1.01	0.70	0.54	0.32
2	0.67	0.45	0.42	0.22

and for various polynomial accuracy levels. It can be seen that the right order of magnitude of the flux at the traces is seized already with the lowest order of accuracy. The flux balance results for all orders show again a perfect match between the total incoming flow through the source fractures (equal to a total flux of 400, given by the boundary conditions) and the flux entering the sink fracture through its traces, with a mismatch near to the machine-error order of magnitude.

Table 7
DFN134: flux entering the sink fracture through its traces for various polynomial accuracy levels, $\delta = 3.68$.

Local trace	Order 0	Order 1	Order 2
Γ_1	7.7695	8.7141	7.9296
Γ_2	22.6830	22.7356	22.6577
Γ_3	44.1668	45.9451	41.8777
Γ_4	20.9764	25.6750	31.8235
Γ_5	4.2227	3.3396	3.0034
Γ_6	1.2128	1.1298	1.5661
Γ_7	141.0733	142.6016	142.8069
Γ_8	97.4382	90.4480	89.2446
Γ_9	43.0454	45.2085	44.6129
Γ_{10}	17.4119	14.2027	14.4776
Balance	400.0000	400.0000	400.0000

6. Conclusions

In the present work a numerical method for the resolution of the advection-diffusion-reaction problem in mixed form in network of fractures is proposed. The method exploits the flexibility of virtual elements in handling almost general polygonal meshes to easily generate a conforming mesh of the network. Suitable approximation spaces are introduced, and the well posedness of the resulting numerical scheme is shown.

Benchmark problems are proposed on simple networks with known analytic solutions, showing optimal convergence properties for the method for discrete spaces of increasing polynomial accuracy ranging from 0 to 5. Qualitative results on more complex networks show good approximation performances already for the lower polynomial accuracy levels. The direct computation of the velocity variable allows for a very accurate description of the flux, which is of paramount importance in view of the use of such velocity field as an input for simulations of dispersion phenomena.

References

[1] M.C. Cacas, E. Ledoux, G. de Marsily, B. Tillie, A. Barbreau, E. Durand, B. Feuga, P. Peaudecerf, Modeling fracture flow with a stochastic discrete fracture network: calibration and validation: 1. The flow model, Water Resour. Res. 26 (1990) 479–489. http://dx.doi.org/10.1029/WR026i003p00479.

[2] A.W. Nordqvist, Y.W. Tsang, C.F. Tsang, B. Dverstop, J. Andersson, A variable aperture fracture network model for flow and transport in fractured rocks, Water Resour. Res. 28 (1992) 1703–1713. http://dx.doi.org/10.1029/92WR00216.

[3] W.S. Dershowitz, C. Fidelibus, Derivation of equivalent pipe networks analogues for three-dimensional discrete fracture networks by the boundary element method, Water Resour. Res. 35 (1999) 2685–2691. http://dx.doi.org/10.1029/1999WR900118.

[4] C. Fidelibus, The 2d hydro-mechanically coupled response of a rock mass with fractures via a mixed BEM-FEM technique, Int. J. Numer. Anal. Methods Geomech. 31 (11) (2007) 1329–1348.

[5] V. Lenti, C. Fidelibus, A bem solution of steady-state flow problems in discrete fracture networks with minimization of core storage, Comput. Geosci. 29 (9) (2003) 1183–1190. http://dx.doi.org/10.1016/S0098-3004(03)00140-7.

[6] S.P. Neuman, Trends, prospects and challenges in quantifying flow and transport through fractured rocks, Hydrogeol. J. 13 (1) (2005) 124–147. http://dx.doi.org/10.1007/s10040-004-0397-2.

[7] J. Hyman, C. Gable, S. Painter, N. Makedonska, Conforming delaunay triangulation of stochastically generated three dimensional discrete fracture networks: a feature rejection algorithm for meshing strategy, SIAM J. Sci. Comput. 36 (2014) A1871–A1894. http://dx.doi.org/10.1137/130942541.

[8] J.D. Hyman, S. Karra, N. Makedonska, C.W. Gable, S.L. Painter, H.S. Viswanathan, dfnworks: a discrete fracture network framework for modeling subsurface flow and transport, Comput. Geosci. 84 (2015) 10–19. http://dx.doi.org/10.1016/j.cageo.2015.08.001.

[9] N. Makedonska, S.L. Painter, Q.M. Bui, C.W. Gable, S. Karra, Particle tracking approach for transport in three-dimensional discrete fracture networks, Comput. Geosci. 19 (5) (2015) 1123–1137. http://dx.doi.org/10.1007/s10596-015-9525-4.

[10] B. Nœtinger, N. Jarrige, A quasi steady state method for solving transient Darcy flow in complex 3D fractured networks, J. Comput. Phys. 231 (1) (2012) 23–38. http://dx.doi.org/10.1016/j.jcp.2011.08.015.

[11] B. Nœtinger, A quasi steady state method for solving transient Darcy flow in complex 3D fractured networks accounting for matrix to fracture flow, J. Comput. Phys. 283 (2015) 205–223. http://dx.doi.org/10.1016/j.jcp.2014.11.038.

[12] C. D'Angelo, A. Scotti, A mixed finite element method for Darcy flow in fractured porous media with non-matching grids, ESAIM: M2AN 46 (2) (2012) 465–489. http://dx.doi.org/10.1051/m2an/2011148.

[13] L. Formaggia, A. Fumagalli, A. Scotti, P. Ruffo, A reduced model for Darcy's problem in networks of fractures, ESAIM: Math. Model. Numer. Anal. 48 (4) (2014) 1089–1116. http://dx.doi.org/10.1051/m2an/2013132.

[14] B. Schwenck, N. Flemisch, R. R. Helmig, B. Wohlmuth, Dimensionally reduced flow models in fractured porous media: crossings and boundaries, Comput. Geosci. 19 (6) (2015) 1219–1230.

[15] H. Huang, T.A. Long, J. Wan, W.P. Brown, On the use of enriched finite element method to model subsurface features in porous media flow problems, Comput. Geosci. 15 (4) (2011) 721–736. http://dx.doi.org/10.1007/s10596-011-9239-1.

[16] S. Berrone, S. Pieraccini, S. Scialò, A. PDE-constrained, A PDE-constrained optimization formulation for discrete fracture network flows, SIAM J. Sci. Comput. 35 (2) (2013) B487–B510. http://dx.doi.org/10.1137/120865884.

[17] S. Berrone, S. Pieraccini, S. Scialò, On simulations of discrete fracture network flows with an optimization-based extended finite element method, SIAM J. Sci. Comput. 35 (2) (2013) A908–A935. http://dx.doi.org/10.1137/120882883.

[18] S. Berrone, S. Pieraccini, S. Scialò, An optimization approach for large scale simulations of discrete fracture network flows, J. Comput. Phys. 256 (2014) 838–853. http://dx.doi.org/10.1016/j.jcp.2013.09.028.

[19] S. Berrone, C. Canuto, S. Pieraccini, S. Scialò, Uncertainty quantification in discrete fracture network models: stochastic fracture transmissivity, Comput. Math. Appl. 70 (4) (2015) 603–623. http://dx.doi.org/10.1016/j.camwa.2015.05.013.

[20] S. Berrone, S. Pieraccini, S. Scialò, Non-stationary transport phenomena in networks of fractures: effective simulations and stochastic analysis, Comput. Methods Appl. Mech. Eng. 315 (2017) 1098–1112. http://dx.doi.org/10.1016/j.cma.2016.12.006.

[21] S. Berrone, S. Pieraccini, S. Scialò, F. Vicini, A parallel solver for large scale DFN flow simulations, SIAM J. Sci. Comput. 37 (3) (2015) C285–C306. http://dx.doi.org/10.1137/140984014.

[22] S. Berrone, S. Pieraccini, S. Scialò, Towards effective flow simulations in realistic discrete fracture networks, J. Comput. Phys. 310 (2016) 181–201. http://dx.doi.org/10.1016/j.jcp.2016.01.009.

[23] S. Pieraccini, S. Scialò, On a PDE-constrained optimization approach for flow simulations in fractured media, in: Advances in Discretization Methods, Vol. 12 of SEMA SIMAI Springer Series, Springer International Publishing, Switzerland, 2016, pp. 27–45.

[24] M.F. Benedetto, S. Berrone, S. Pieraccini, S. Scialò, The virtual element method for discrete fracture network simulations, Comput. Methods Appl. Mech. Eng. 280 (0) (2014) 135–156. http://dx.doi.org/10.1016/j.cma.2014.07.016.

[25] L. Beirão da Veiga, K. Lipnikov, G. Manzini, The Mimetic Finite Difference Method for Elliptic Problems, Vol. 11 of Modeling, Simulation & Applications, Springer, 2014.

[26] K. Lipnikov, G. Manzini, M. Shashkov, Mimetic finite difference method, J. Comput. Phys. 257 (2014) 1163–1227.

[27] O. Al-Hinai, S. Srinivasan, M.F. Wheeler, Mimetic finite differences for flow in fractures from microseismic data, in: SPE Reservoir Simulation Symposium, Society of Petroleum Engineers, 2015.

[28] P.F. Antonietti, L. Formaggia, A. Scotti, M. Verani, N. Verzott, Mimetic finite difference approximation of flows in fractured porous media, ESAIM: Math. Model. Numer. Anal. 50 (3) (2016) 809–832. http://dx.doi.org/10.1051/m2an/2015087.

[29] L. Beirão da Veiga, F. Brezzi, L.D. Marini, A. Russo, The hitchhiker's guide to the virtual element method, Math. Model. Methods Appl. Sci. 24 (8) (2014) 1541–1573.

[30] F. Brezzi, R.S. Falk, L.D. Marini, Basic principles of mixed virtual element methods, ESAIM: Math. Model. Numer. Anal. 48 (4) (2014) 1227–1240. http://dx.doi.org/10.1051/m2an/2013138.

[31] L. Beirão da Veiga, F. Brezzi, L.D. Marini, A. Russo, Virtual element methods for general second order elliptic problems on polygonal meshes, Math. Model. Methods Appl. Sci. 26 (04) (2015) 729–750. http://dx.doi.org/10.1142/S0218202516500160.

[32] L. Beirão da Veiga, F. Brezzi, L.D. Marini, A. Russo, Mixed virtual element methods for general second order elliptic problems on polygonal meshes, ESAIM: Math. Model. Numer. Anal. 50 (3) (2016) 727–747. http://dx.doi.org/10.1051/m2an/2015067.

[33] M.F. Benedetto, S. Berrone, A. Borio, S. Pieraccini, S. Scialò, Order preserving SUPG stabilization for the virtual element formulation of advection-diffusion problems, Comput. Methods Appl. Mech. Eng. 311 (2016) 18–40. http://dx.doi.org/10.1016/j.cma.2016.07.043.

[34] S. Berrone, A. Borio, Orthogonal polynomials in badly shaped polygonal elements for the Virtual Element Method, Finite Elem. Anal. Des. 129 (2017) 14–31. http://dx.doi.org/10.1016/j.finel.2017.01.006.

[35] M.F. Benedetto, S. Berrone, S. Scialò, A globally conforming method for solving flow in discrete fracture networks using the virtual element method, Finite Elem. Anal. Des. 109 (2016) 23–36. http://dx.doi.org/10.1016/j.finel.2015.10.003.

[36] M.F. Benedetto, S. Berrone, A. Borio, The Virtual Element Method for underground flow simulations in fractured media, in: Advances in Discretization Methods, Vol. 12 of SEMA SIMAI Springer Series, Springer International Publishing, Switzerland, 2016, pp. 167–186. http://dx.doi.org/10.1007/978-3-319-41246-7_8.

[37] V. Martin, J. Jaffré, J.E. Roberts, Modeling fractures and barriers as interfaces for flow in porous media, SIAM J. Sci. Comput. 26 (5) (2005) 1667–1691. http://dx.doi.org/10.1137/S1064827503429363.

[38] A. Fumagalli, A. Scotti, A numerical method for two-phase flow in fractured porous media with non-matching grids, Adv. Water Resour. 62 (2013) 454–464. http://dx.doi.org/10.1016/j.advwatres.2013.04.001.

[39] G. Pichot, J. Erhel, J. de Dreuzy, A mixed hybrid mortar method for solving flow in discrete fracture networks, Appl. Anal. 89 (2010) 1629–1643. http://dx.doi.org/10.1080/00036811.2010.495333.

[40] G. Pichot, J. Erhel, J. de Dreuzy, A generalized mixed hybrid mortar method for solving flow in stochastic discrete fracture networks, SIAM J. Sci. Comput. 34 (2012) B86–B105. http://dx.doi.org/10.1137/100804383.

[41] M. Vohralík, J. Maryška, O. Severýn, Mixed and nonconforming finite element methods on a system of polygons, Appl. Numer. Math. 51 (2007) 176–193.

[42] O. Al-Hinai, S. Srinivasan, M.F. Wheeler, Domain decomposition for flow in porous media with fractures, in: SPE Reservoir Simulation Symposium, 23–25 February 2013, Houston, Texas, USA, Society of Petroleum Engineers, 2015. ⟨http://dx.doi.org/10.2118/173319-MS⟩.

[43] J. Douglas Jr., J.E. Roberts, Global estimates for mixed methods for second order elliptic equations, Math. Comp. 44 (1985) 39–52.

[44] E. Cáceres, G.N. Gatica, A mixed virtual element method for the pseudostress-velocity formulation of the stokes problem, IMA J. Numer. Anal. 37 (1) (2017) 296. http://dx.doi.org/10.1093/imanum/drw002.

[45] L. Beirão da Veiga, F. Brezzi, L.D. Marini, A. Russo, H(div) and h(curl)-conforming virtual element methods, Numer. Math. 133 (2) (2016) 303–332. http://dx.doi.org/10.1007/s00211-015-0746-1.

[46] L. Beirão da Veiga, F. Brezzi, L.D. Marini, A. Russo, Virtual element implementation for general elliptic equations, Springer Int. Publ. Cham (2016) 39–71. http://dx.doi.org/10.1007/978-3-319-41640-3_2.

[47] T. Arbogast, L.C. Cowsar, M.F. Wheeler, I. Yotov, Mixed finite element methods on nonmatching multiblock grids, SIAM J. Numer. Anal. 37 (4) (2000) 1295–1315.

[48] O.C. Zienkiewicz, S. Qu, R.L. Taylor, S. Nakazawa, The patch test for mixed formulations, Int. J. Numer. Methods Eng. 23 (10) (1986) 1873–1883. http://dx.doi.org/10.1002/nme.1620231007.

[49] I. Babuška, R. Narasimhan, The babuška-brezzi condition and the patch test: an example, Comput. Methods Appl. Mech. Eng. 140 (1–2) (1997) 183–199. http://dx.doi.org/10.1016/S0045-7825(96)01058-4.

[50] R. Glowinski, M.F. Wheeler, Domain decomposition and mixed finite element methods for elliptic problems, in: Proceedings of the First international symposium on domain decomposition methods for partial differential equations, 1998, pp. 144–172.